nature materials

Article

https://doi.org/10.1038/s41563-023-01716-9

Cell volume expansion and local contractility drive collective invasion of the basement membrane in breast cancer

Received: 18 June 2022

Accepted: 5 October 2023

Published online: 13 November 2023

Check for updates

Julie Chang[1,12], Aashrith Saraswathibhatla[2,12], Zhaoqiang Song[3,4], Sushama Varma[5], Colline Sanchez[6,7], Naomi Hassan Kahtan Alyafei[1], Dhiraj Indana[2], Raleigh Slyman[2], Sucheta Srivastava[5], Katherine Liu[8], Michael C. Bassik[8], M. Peter Marinkovich[9,10], Louis Hodgson[6,7], Vivek Shenoy[3,4], Robert B. West[5] & Ovijit Chaudhuri[2,11]

Breast cancer becomes invasive when carcinoma cells invade through the basement membrane (BM)—a nanoporous layer of matrix that physically separates the primary tumour from the stroma. Single cells can invade through nanoporous three-dimensional matrices due to protease-mediated degradation or force-mediated widening of pores via invadopodial protrusions. However, how multiple cells collectively invade through the physiological BM, as they do during breast cancer progression, remains unclear. Here we developed a three-dimensional in vitro model of collective invasion of the BM during breast cancer. We show that cells utilize both proteases and forces—but not invadopodia—to breach the BM. Forces are generated from a combination of global cell volume expansion, which stretches the BM, and local contractile forces that act in the plane of the BM to breach it, allowing invasion. These results uncover a mechanism by which cells collectively interact to overcome a critical barrier to metastasis.

The initial invasion of carcinoma cells through the basement membrane (BM) and into the stromal matrix is a necessary first step to metastasis[1]. The BM is a nanoporous meshwork of extracellular matrix (ECM) proteins that separates epithelial cells from the stromal matrix, acting as a physical barrier to cell invasion[2,3]. In pre-invasive ductal carcinoma in situ (DCIS), mammary epithelial cells undergo aberrant proliferation, but remain confined within the BM; this pre-invasive condition is largely treatable with low mortality[4]. However, once carcinoma cells invade through the BM, the tumour becomes invasive breast carcinoma (IBC) and can undergo metastasis, resulting in increased mortality[5]. This mechanism by which cells collectively invade through the BM is not well understood.

In principle, carcinoma cells can breach the BM through either protease-dependent or force-driven protease-independent modes. It has been established that cells can secrete matrix metalloproteinases (MMPs) to chemically degrade the BM to enable cancer cell invasion into the stromal matrix[6,7]. Specifically, cells can extend protrusions known as invadopodia, which secrete MMPs and express membrane

[1]Department of Bioengineering, Stanford University, Stanford, CA, USA. [2]Department of Mechanical Engineering, Stanford University, Stanford, CA, USA. [3]Center for Engineering Mechanobiology, University of Pennsylvania, Philadelphia, PA, USA. [4]Department of Materials Science and Engineering, University of Pennsylvania, Philadelphia, PA, USA. [5]Department of Pathology, Stanford University Medical Center, Palo Alto, CA, USA. [6]Department of Molecular Pharmacology, Albert Einstein College of Medicine, Bronx, NY, USA. [7]Gruss-Lipper Biophotonics Center, Albert Einstein College of Medicine, Bronx, NY, USA. [8]Department of Genetics, Stanford University Medical Center, Palo Alto, CA, USA. [9]Department of Dermatology, Stanford University School of Medicine, Stanford, CA, USA. [10]Dermatology Service, VA Medical Center, Palo Alto, CA, USA. [11]Chemistry, Engineering, and Medicine for Human Health (ChEM-H), Stanford University, Stanford, CA, USA. [12]These authors contributed equally: Julie Chang, Aashrith Saraswathibhatla. e-mail: chaudhuri@stanford.edu

anchored MMPs[8]. Recent studies reveal that invadopodia and cells can exert forces, without proteolytic degradation, to physically deform, remodel and move through the nanoporous ECM if the ECM exhibits sufficient mechanical plasticity[9–12]. However, most studies of BM invasion focus on individual non-cancer cells or models using an exogenous or reconstituted BM matrix. Moreover, clinical evidence supports that the initial invasion of the BM is driven by collective cells as opposed to individual cells[13,14]. How cancer cells collectively use proteases and/or forces to breach the endogenous BM within a three-dimensionally confining matrix is undescribed.

Using an in vitro three-dimensional (3D) culture model of stiffness-induced invasion of mammary epithelial cells through the endogenous BM, we studied the mechanisms by which cells collectively invade through the BM (Fig. 1a). These data reveal that cells use both protease and force-driven modes of invasion through the BM. Mechanistically, we find that cells synergistically use both global cell volume expansion and localized actomyosin contractility to exert tangential forces on the BM and create openings for cells to migrate through the BM during invasion.

Results

A 3D in vitro model of breast carcinoma invasion

We designed a 3D culture hydrogel model to study collective mammary epithelial cell invasion through the endogenous BM (Fig. 1a,b). Single MCF10A mammary epithelial cells cultured on a layer of reconstituted basement membrane (rBM) proliferated and self-assembled into 3D organotypic acini. These acini exhibited key features observed in mammary ducts, including apicobasal polarity, lumen formation and a layer of endogenous BM on the periphery. These acini were harvested and encapsulated into interpenetrating network (IPN) hydrogels of rBM and alginate. Enhanced mammographic density and correspondingly increased ECM stiffness is one of the strongest risk factors for breast cancer progression and may play a key role in promoting IBC progression (Fig. 1a)[15]. Increased stiffness of the BM itself and the stromal matrix has been shown to promote cell invasion, and subsequently, metastasis[16,17]. IPN stiffness can be modulated to match the stiffness relevant to breast cancer progression through the addition of calcium ions, without changing the protein concentration, matrix architecture or pore size[18]. The calcium used for crosslinking does not impact the phenotype of these cells in the concentration range used[18]. IPNs of two stiffnesses were made: 'soft' and 'stiff' IPNs that mimicked the stiffness of healthy and tumour tissues with elastic moduli of 0.3 and 2.5 kPa, respectively (Fig. 1c)[19,20]. These IPNs exhibited similar degrees of mechanical plasticity and loss tangents (Extended Data Fig. 1a–c). Overall, we developed IPNs of different stiffnesses that maintain similar mechanical plasticity and viscoelastic behaviours.

Next, we evaluated whether an endogenous BM secreted by MCF10A cells resembled in vivo BM by analysing the BM composition and thickness. The endogenous BM contained laminin-332 and collagen-IV (Fig. 1d), in which laminin-332 interfaced with cells on the inner layer of the BM, whereas collagen-IV interfaced with the IPN on the outer layer of the BM, mimicking the localization of laminin and collagen-IV in BM in vivo (Fig. 1d)[3]. Moreover, the thickness of the laminin layer in acini in vitro at day 7 matched the thickness of the laminin layer in DCIS in vivo samples; the laminin layer in normal breast tissue samples was substantially thicker than the laminin layer in DCIS samples (Fig. 1e,f). Transformed cells, such as MCF10AT and MCF10CA1a, did not form a continuous endogenous BM layer (Extended Data Fig. 1d–e). Therefore, the BM formed by MCF10A acini serves as a model of BM in DCIS.

We next evaluated the ability of this 3D model to recapitulate the key features of human breast carcinoma progression. Although the BM separates acini from the IPN, a previous work indicates that cells can sense IPN stiffness through the endogenous BM[21]. In human breast tissue samples, normal ducts appeared round, whereas ducts in IBC exhibited a jagged and irregular morphology (Fig. 1g). In our in vitro model, these two states were captured by stable, round acini with intact BM in soft IPNs and invasive, collectively invading acini with breached BM in stiff IPNs three days after initial encapsulation (Fig. 1h,i and Supplementary Videos 1–4). PI3K inhibition significantly decreased the number of invasive acini (Fig. 1j), suggesting that the invasive phenotype is induced through some of the signalling pathways characteristic of invasive ductal carcinoma. We observed increased acinar area, decreased acinar circularity and decreased BM area/average acini area in stiff IPNs compared with soft IPNs, supporting the finding of increased collective invasion in stiff IPNs (Fig. 1k). The cell–cell junction protein E-cadherin was present in both non-invasive and invasive acini, demonstrating E-cadherin-positive collective invasion in this model, as observed in IBC (Fig. 1l,m). In summary, we developed an in vitro 3D model of increased-stiffness-induced collective invasion of mammary epithelial cells through endogenous BM that captured the key features of IBC.

Protease inhibitors partially inhibit cell invasion

We sought to elucidate whether cells use protease-dependent and/or protease-independent mechanisms to invade through the BM, focusing on the invasive acini observed in stiff IPNs. To ascertain the role of proteases in collective cell invasion, we added broad-spectrum MMP inhibitors to the cell culture media in stiff IPNs[22]. GM6001 and marimastat significantly reduced cell invasion, whereas the protease inhibitor cocktail did not reduce cell invasion (Fig. 2a,b). Still, cell invasion occurred when protease inhibitors were added, indicating that protease inhibitors partially, but do not fully, inhibit cell invasion.

BM accumulates at cell invasion sites

Since protease inhibitors did not fully inhibit cell invasion, we explored the role of physical forces during BM invasion. To visualize the BM movement during collective cell invasion, the endogenous BM was tagged with Alexa Fluor 488-conjugated laminin-332 antibodies, since laminin-332 is specific to cell-secreted BM and the rBM in IPNs lacks this laminin isoform[23]. An indiscernible amount of additional BM was secreted by cells before and after acini IPN encapsulation (Extended Data Fig. 1f). The inward movement of the BM into the acini centre where the BM was breached, with cells migrating into the surrounding IPN, was observed (Fig. 2c and Supplementary Video 5). There was an overall decrease in the BM volume after cells invaded through the BM and

Fig. 1 | Increased stiffness induces collective invasion through endogenous BM in a 3D culture model of IBC. a, Schematic of breast carcinoma progression. **b**, Schematic of a 3D in vitro model of breast carcinoma progression, in which preformed organotypic MCF10A acini are encapsulated into soft or stiff alginate-rBM IPNs. **c**, Young's modulus of soft and stiff alginate-rBM IPNs ($N = 3–6$ gels). **d**, Collagen-IV (red), laminin-332 (green) and DAPI (blue) staining of the endogenous BM structure in MCF10A acini. **e**, Laminin-332 (red) and DAPI (blue) staining in normal and DCIS in vivo breast tissue samples. **f**, Laminin thickness of in vitro acini and in vivo DCIS and normal samples ($N = 12$ in vitro samples, $N = 32$ in vivo DCIS samples, $N = 45$ in vivo normal samples). **g**, Haematoxylin and eosin images of normal (top) and IBC (bottom) in vivo breast tissue samples. The black arrow points to collectively invading cells. **h**, Laminin-332 (red), actin (green) and DAPI (blue) staining of MCF10A acini in soft and stiff IPNs (left). Traces of acini in soft and stiff IPNs (right). The white arrow indicates collective cell invasion through the BM. **i**, Percentage of invasive acini in soft and stiff IPNs ($N = 4–6$ different gels). **j**, Percentage of invasive acini in stiff IPNs with control or PI3K inhibitor ($N \geq 30$ acini in 3–6 hydrogels). **k**, Quantification of acini circularity, acini area and BM/average acini area in soft and stiff IPNs ($N \geq 30$ acini in 3–6 different gels). **l**, DAPI (blue) and E-cadherin (red) staining in soft and stiff IPNs. **m**, E-cadherin (green) and DAPI (blue) staining in normal, DCIS and IBC in vivo breast tissue samples. For the data in **c**, **i** and **j**, a two-sided unpaired *t*-test was performed. One-way analysis of variance (ANOVA) with Tukey's correction for multiple comparisons was performed for the data in **f**. A two-sided Welch's *t*-test was performed for the data in **k**. Scale bars, 20 μm (**d**, **l**), 100 μm (**e**, **g**, **m**), 50 μm (**h**).

https://doi.org/10.1038/s41563-023-01716-9

sequentially exited through the opening, thereby reducing the number of cells contained within the BM over time (Extended Data Fig. 2). Increased laminin accumulation was detected around the breaching site, showing a physical densification of the BM layer around the opening where cells invaded through (Fig. 2d–f and Supplementary Video 6). The increase in the BM signal demonstrates a cell-driven

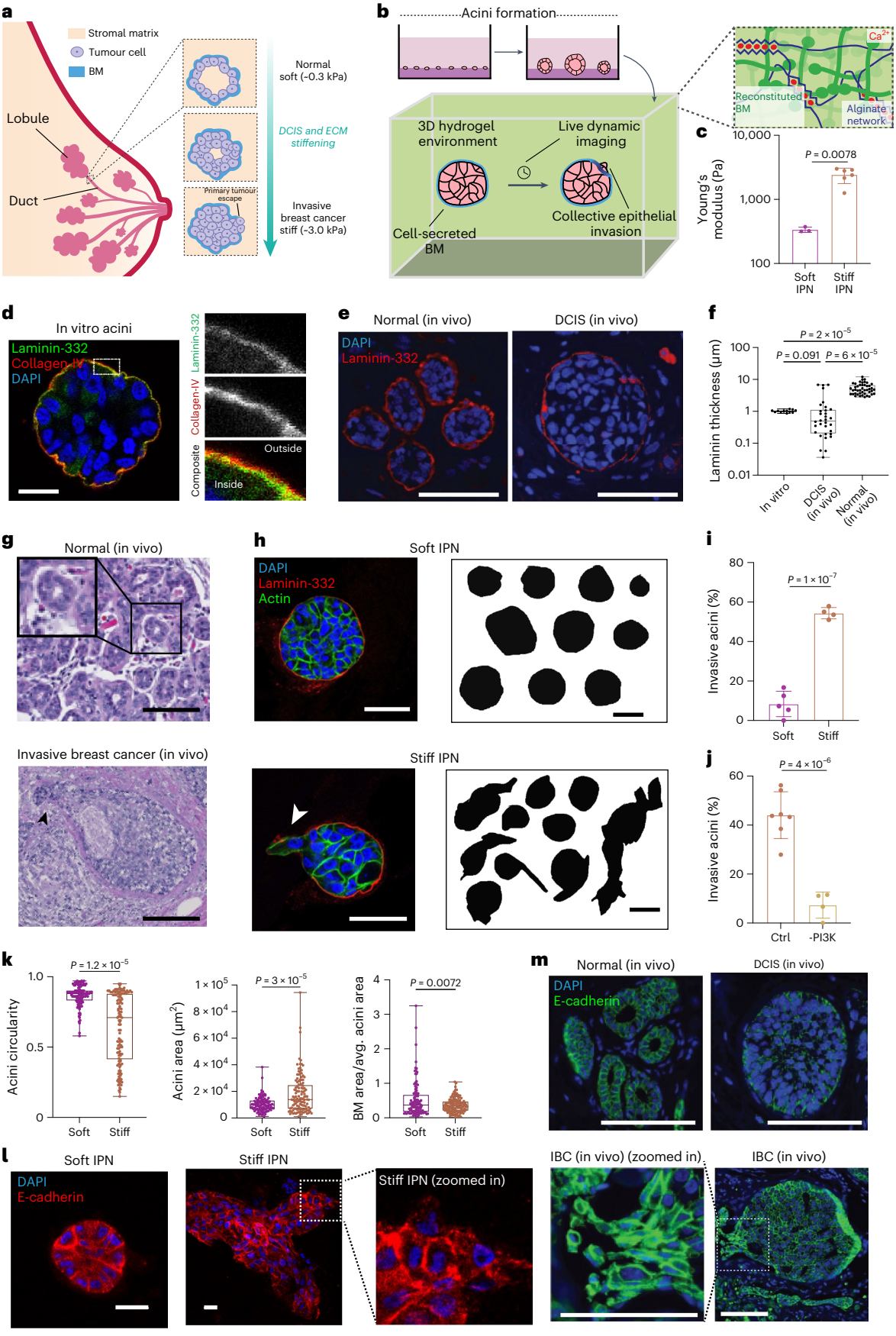

physical accumulation of BM, rather than a loss of BM signal due to protease degradation. Further, the accumulation of BM around the invasion resulted in permanent holes on cell lysing, suggesting that BM exhibits mechanical plasticity (Fig. 2g). Indeed, the hypotonic volume expansion of acini, followed by cell lysing, confirmed BM plasticity (Extended Data Fig. 3 and Supplementary Note 1). Together, these results show that BM invasion is associated with BM accumulation and densification, implicating cell-generated forces.

To establish whether BM densification and deformation resulted from cell-generated forces, we examined the role of actin cytoskeleton activity in BM invasion. Actin densification occurred at the site of BM densification, suggesting that active forces are being generated by cells from the actin cytoskeleton around the BM (Fig. 2h and Supplementary Videos 7 and 8). Focal adhesion kinase (FAK), a key signalling molecule that mediates actomyosin contractility through integrin-based adhesions, accumulated in its phosphorylated form at the boundaries of BM opening in invasive acini (Fig. 2i)[24]. An increased accumulation of phosphorylated FAK (pFAK) was also detected in invasive collective cells that have already breached the BM and invaded into the surrounding IPN (Fig. 2i). The addition of a FAK inhibitor in stiff IPNs decreased both cell invasions with no BM breaching (Fig. 2j). This suggests that force transfer through integrins is associated with initial BM breaching and post-BM breaching cell invasion. pFAK remained present on PI3K inhibition, indicating that pFAK acted upstream of PI3K (Extended Data Fig. 4a,b). Together, our model demonstrated that collective cells use both proteases and forces to plastically deform and breach endogenous BM.

Invadopodial protrusions do not drive BM invasion

To investigate the mechanisms by which cells invade through the BM, we examined the role of invadopodial protrusions, which are known to drive single-cell invasion[9,25,26]. Invadopodial protrusions are actin-rich protrusions that display Tks5 and cortactin, are oscillatory with a lifetime on the order of hours and deliver both proteases and forces onto the matrix to lead invasion. Comparison of collectively invading cells in MCF10A acini with invadopodia-mediated invasion by single MCF10A cells and MDA-MB-231 cells showed striking differences in the invasive behaviour (Fig. 3a–c). Invadopodial protrusions were not observed in collectively invading cells in this hydrogel system; instead, broader protrusions were formed, with invadopodia widths significantly narrower than the invading edge of collectively invading cells (Fig. 3d). To further test the role of invadopodia in collective invasion, Tks5 and cortactin—two key proteins involved in invadopodia protrusions—were evaluated. Immunohistochemistry shows that cortactin localizes to the periphery of the invasive clusters (Fig. 3e). CRISPR/Cas9 knockout of Tks5 in MCF10A reduced invasion compared with the control cells (Fig. 3f–h). These results suggest that although individual invadopodia protrusions are not observed in collective cell invasion, Tks5 and cortactin may still play a role in a different type of invasive structure.

Global cell volume expansion mediates invasion

As invadopodia do not mediate collective invasion, we investigated cell volume expansion as a potential mediator of collective invasion through the BM. Recent studies have demonstrated the involvement of cell volume changes in mechanotransduction, and an increase in cell volume was found to be associated with invasion in a breast cancer 3D culture model without an endogenous BM[27–30]. Increase in the cross-sectional area of acini and BM-enclosed area, expected to be correlated with volume, occurred before BM-breaching events (Fig. 4a). After BM breaching, the BM area decreased, whereas the acini area continued to increase (Fig. 4a). The inhibition of cell proliferation with mitomycin C decreased invasive events, although invasion still occurred (Extended Data Fig. 4c). These observations motivated the analyses of cell volumes of invasive and non-invasive acini in stiff and soft IPNs, respectively. The overall acini volumes in invading acini in stiff IPNs were greater than those in non-invading acini in soft IPNs (Fig. 4b,c). Individual cell volumes were analysed and found to be greater in invading acini in stiff IPNs compared with non-invading acini in soft IPNs. Local changes in cell volume in the invasive front compared with the non-invasive region of the cluster were not observed, and nuclear volumes were similar across all conditions (Extended Data Fig. 4d,e). These findings demonstrate that cell volume expansion is associated with invasion.

Next, we tested the role of cell volume expansion in driving invasion. Transient receptor potential vanilloid-4 (TRPV4) is a stretch-activated ion channel that has been shown to mediate cell volume expansion through the regulation of osmolality of calcium ions in the cytoplasm[28,31]. Volumes of invasive acini in stiff IPNs were greater than the volumes of acini in stiff IPNs treated with GSK205, an inhibitor of TRPV4 (Fig. 4c). The average cell volumes within the invasive acini in stiff IPNs were also greater than the average cell volume in stiff IPNs treated with GSK205 (Fig. 4d). Treatment of acini in stiff IPNs with GSK205 decreased both the percentage of invasive cells and the percentage of breached BM (Fig. 4e). Cell volume expansion was also inhibited by applying osmotic pressure to the acini through the addition of 400 Da polyethylene glycol (PEG) into the cell culture media[28]. Increasing the PEG concentration in the media decreased the percentage of invasive acini (Fig. 4f), collective cell invasion and BM breaching (Fig. 4g). Further, cell areas increased from normal to DCIS and IBC conditions in vivo over a similar range (Fig. 4h), matching the finding that cell volumes are smaller in non-invasive acini compared with invasive acini. However, since the cell volume was not significantly different between DCIS and IBC, we examined other factors promoting the invasive transition.

Experiments to perturb cell–cell adhesions demonstrated that cell collectivity is another factor necessary for BM and cell invasion. Blocking cell–cell adherens junction protein E-cadherin with DECMA-1, confirmed by staining for α-catenin and β-catenin (Extended Data Fig. 5a,d), reduced the collective cell invasion and BM breaching (Fig. 4i,j). Next, we targeted gap junctions, which enable the exchange of ions and fluid between the cells and have been shown to regulate cell volume[32]. Inhibiting gap junctions with carbenoxolone reduced BM breaching (Fig. 4k,l and Extended Data Fig. 5e). CRISPR/Cas9 knockout of connexin 43, a gap junction protein involved in maintaining the polarity of MCF10A (ref. 33) and in controlling the collective invasion through intercellular communication[34], decreased invasion and increased acini circularity (Extended Data Fig. 5f–g). These perturbations indicate the importance of cell–cell adhesions and gap junctions in BM breaching and cell invasion.

Fig. 2 | Collectively invading acini use a combination of both proteases and force to breach the BM. a, Percentage of invasive acini with control, GM6001, marimastat or protease cocktail inhibitor ($N = 6–8$ gels). **b**, Representative bright-field images of invasive acini with MMP inhibitors. **c**, Time-lapse images of an acini with the endogenous BM exhibiting cell invasion and BM breaching. The green arrow points to BM breaching. The white dotted box points to cell invasion. **d**, Bright-field image of invasive acini with the BM in cyan. Horizontal and angled views of the BM from the time-lapse images (shown on an inferno colour scale). **e**, Fluorescent images of BM in invasive acini over 15 h. The intensity of laminin of the yellow cross-section line is plotted. **f**, Fold increase in normalized, with the maximum laminin signal from 0 to 15 h ($N = 10$ acini). **g**, Addition of latrunculin, a potent actin depolymerizer, after cells have invaded the BM demonstrates BM plasticity. Actin (red) and BM (inferno). **h**, Actin signal of MCF10A-RFP-LifeAct acini over 20 h. Actin (viridis) and BM (cyan). The zoomed-in area is shown in the bottom row. **i**, pFAK and laminin-332 in stiff IPNs. The composite image shows pFAK (yellow), laminin-332 (red), actin (green) and nuclei (blue). The green arrows point to a hole in the BM layer. The cyan dotted line outlines the breached BM. **j**, Percentage of invasive acini, cell area, cell circularity and BM area/average cell area in stiff IPNs with control and FAK inhibitor ($N = 3$ gels or $N \geq 30$ acini in three gels). One-way ANOVA was performed for the data in **a**. A two-sided Welch's test was performed for the data in **j**. One-sample *t*-test was performed for the data in **f**. Scale bars, 50 μm (**b**, **c**, **i**), 20 μm (**d**, **e**), 25 μm (**g**, **h**).

https://doi.org/10.1038/s41563-023-01716-9

α3β1 integrin and actomyosin contractility drive invasion

Next, we explored the role of cell-generated contractile forces in BM breaching and invasion. Contractile forces from cells are generated by the actomyosin network and exerted on the surrounding BM α3β1 integrin attachment to the α-chain of laminin in the BM[3,35]. The addition of anti-laminin α3 antibodies to the culture media decreased the percentage of invasive acini and breached BM in stiff IPNs (Fig. 5a,b). Further, the inhibition of α3 and β1 integrins separately and together significantly reduced the percentage of invasive acini (Fig. 5c,d).

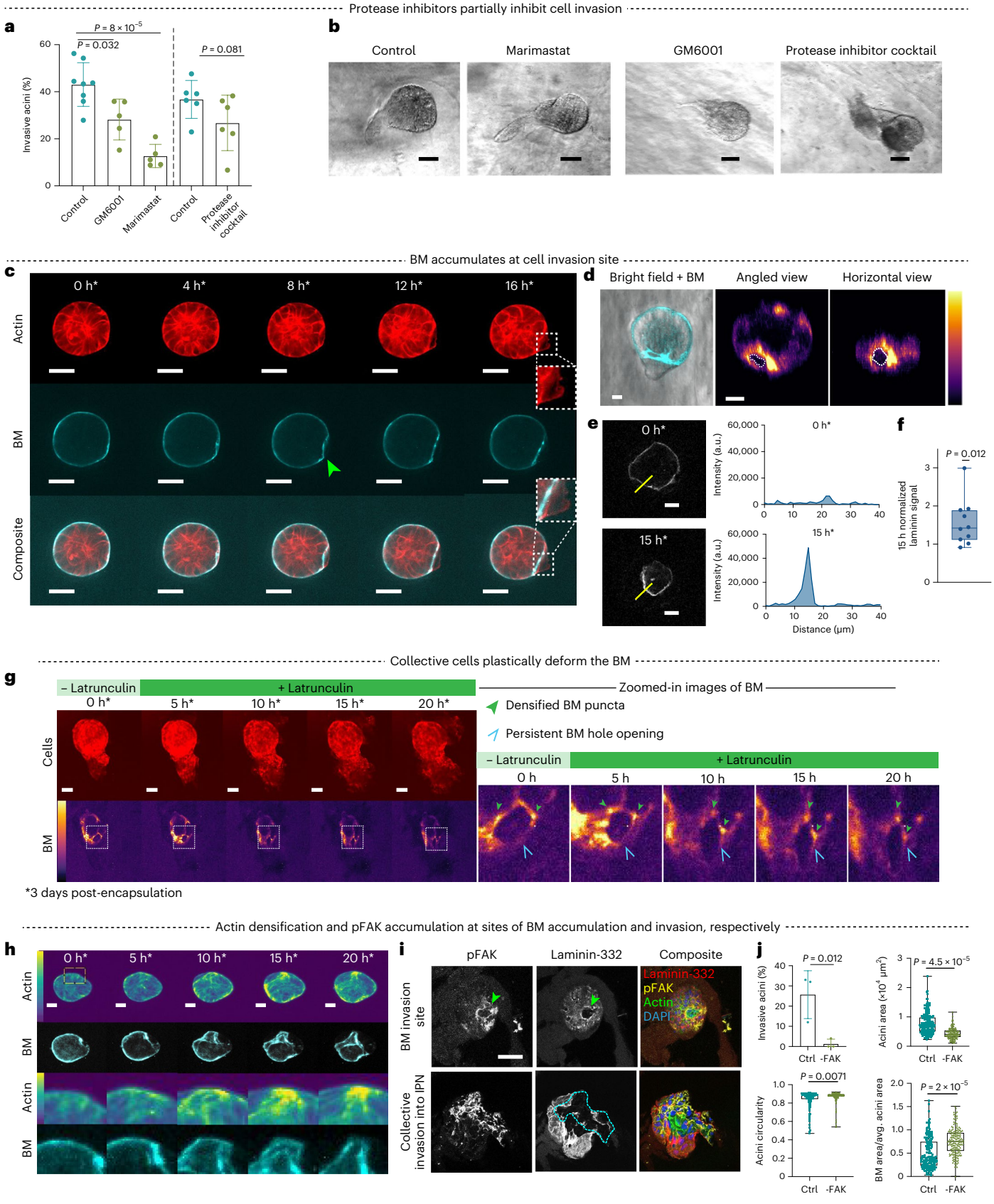

https://doi.org/10.1038/s41563-023-01716-9

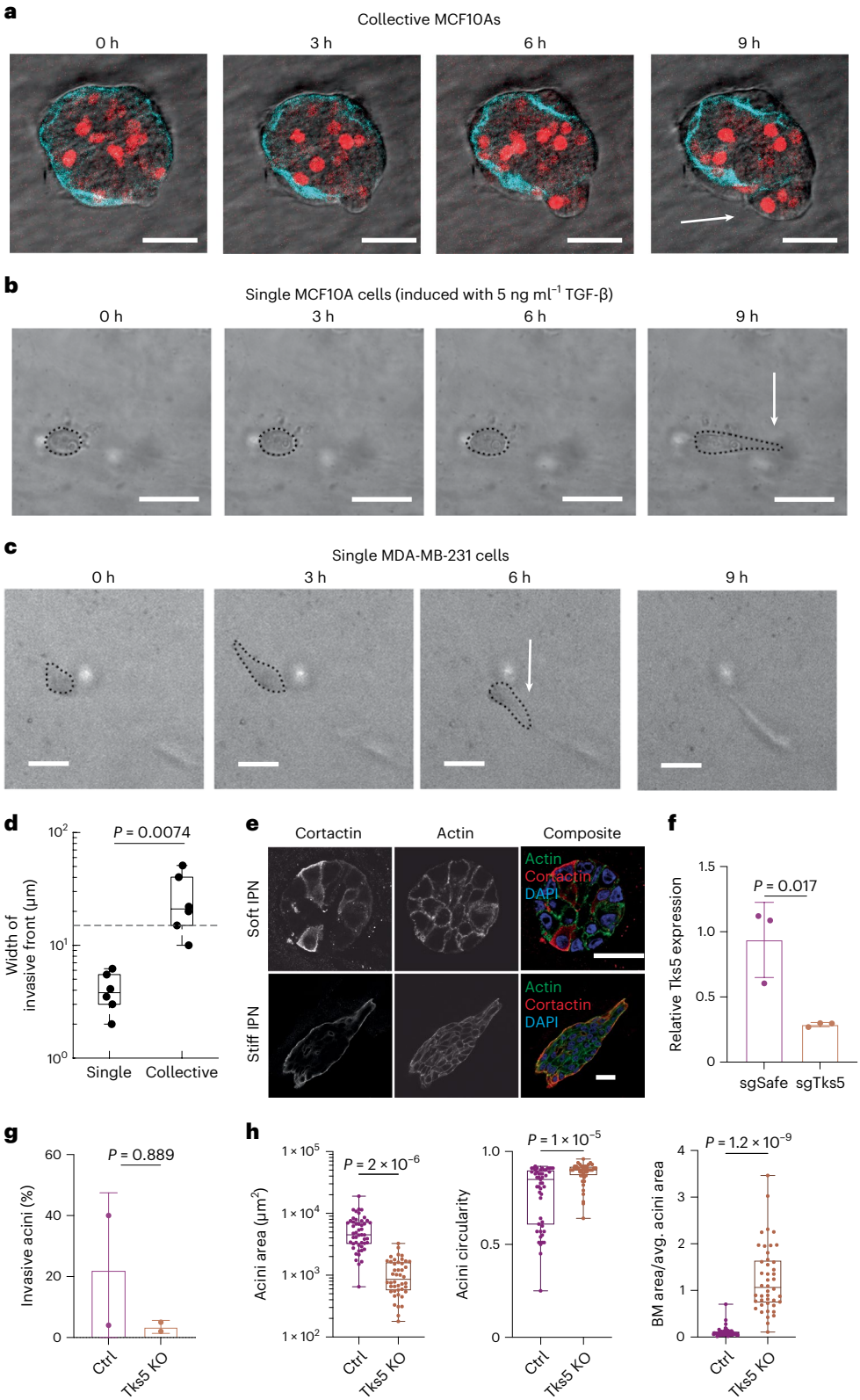

Fig. 3 | Single cells extend invadopodia-like protrusions during invasions whereas collectively invading acini do not. a, Representative image of a collective cluster of cells of an acini invading in a stiff IPN. The arrow points to collectively migrating cells. Cyan, BM; red, cell nuclei. **b**, Representative phase images of a single MCF10A cell migrating in a stiff IPN. The arrow shows the protrusion of the cell. **c**, Representative phase-contrast images of a single MDA-MB-231 cell migrating in a stiff IPN. The arrow indicates the protrusion of the cell. **d**, Width of the invading front of single cells compared with collective cells ($N = 6$ cells or acini in three gels). **e**, Cortactin (red), actin (green) and DAPI (blue) staining in acini of soft and stiff IPNs. **f**, Reverse-transcription polymerase chain reaction of sgTks5 and sgSafe guides used in CRISPR Cas9 MCF10As ($N = 3$ gels). **g**, Percentage of invasive acini in control and CRISPR Tks5 KO acini ($N = 2$ gels). **h**, Acini area, acini circularity and BM area/average acini area of control and CRISPR Tks5 KO acini in stiff IPNs ($N \geq 30$ acini from two gels). Two-sided Welch's test was performed for the data in **d** and **f**–**h**. Scale bars, 25 μm (**a**–**c**, **e**).

https://doi.org/10.1038/s41563-023-01716-9

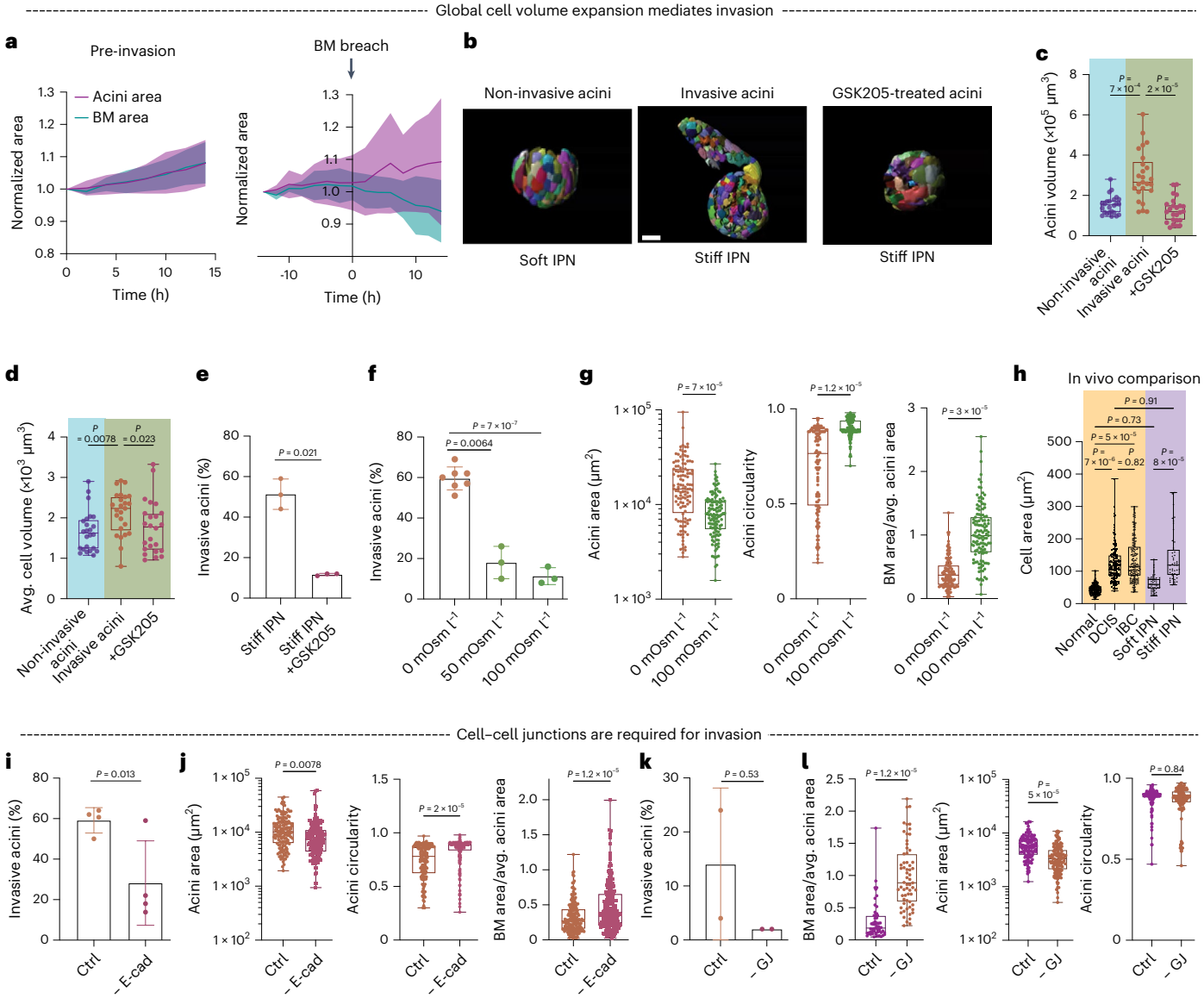

Fig. 4 | Global cell volume expansion and cell–cell junctions are required for invasion. a, Normalized area of acini (purple) and BM (blue) during pre-BM invasion (left) and BM breaching (right). **b**, Representative Imaris renderings of invasive acini, non-invasive acini and GSK205-treated acini. Blue denotes soft IPN and green denotes stiff IPN. **c**, Acini volume of invasive acini, non-invasive acini and GSK205-treated acini ($N \geq 20$ acini from 3–6 gels). **d**, Average cell volumes of invasive acini, non-invasive acini and GSK205-treated acini ($N \geq 20$ acini from 3–6 gels). **e**, Percentage of invasive cell membranes in stiff IPNs and stiff IPN with GSK205 ($N = 3$ gels). **f**, Percentage of invasive acini in stiff IPNs with varying osmotic pressures ($N = 3$–7 gels). **g**, Acini area, acini circularity and BM area/average acini area in stiff IPN with 0 and 100 mOsm l^{-1} osmotic pressure ($N \geq 30$ acini from 3–6 gels). **h**, Cell area based on E-cadherin stains in human breast tissue samples of normal, DCIS and IBC conditions. $N \geq 3$ samples. Orange denotes in vivo and purple denotes in vitro. **i**, Percentage of invasive acini in stiff IPNs with E-cadherin function-blocking antibody ($N = 4$ gels). **j**, Acini area, acini circularity and BM area/average acini area in stiff IPN with control or E-cadherin function-blocking antibody ($N > 30$ acini in four gels). **k**, Percentage of invasive acini in stiff IPNs with gap junction inhibitor ($N = 2$ gels). **l**, Acini area, acini circularity and BM area/average acini area in stiff IPN with control or gap junction inhibitor ($N \geq 30$ acini in two gels). Two-sided Welch's test was performed for the data in **e**, **g** and **i**–**l**. Kruskal–Wallis with Dunn's multiple comparisons test was performed for the data in **c** and **d**. One-way ANOVA was performed for the data in **f**, and one-way ANOVA with Tukey's multiple comparisons test was performed for the data in **h**. Scale bar, 25 µm (**b**).

After finding the role of the integrin–laminin link on mediating invasion, we examined the role of actomyosin-based contractility. The quantification of the average myosin IIa/actin ratio pointed to increased staining of myosin IIa in stiff IPNs, suggesting increased acini contractility in stiff IPNs (Fig. 5e,f). The inhibition of myosin light chain kinase, myosin II, Rho GTPase and actin polymerization demonstrated a reduction in cell invasion and BM invasion (Fig. 5g,h). The activation of RhoA was directly examined using a RhoA Förster resonance energy transfer (FRET) biosensor to detect active RhoA (Fig. 5i,j)[36]. An initially high RhoA FRET signal around the area of BM invasion was observed and followed by a sharp decrease after the BM hole opened. The RhoA signal around the area of BM densification was higher than the RhoA signal around a non-breached area in the BM (Fig. 5j). This suggests that Rho-activated contractility is involved in the initial formation of a hole in the BM, followed by a relaxation back to the baseline. Together, these experiments illustrate the role of cell contractility in BM breaching and collective cell invasion.

Collectively invading cells exert tangential forces on the BM

We next explored the biophysical mechanism through which cells tear the BM to initiate invasion. The 3D deformations of the BM showed local regions of large local deformations (Fig. 5k and Supplementary Video 11).

https://doi.org/10.1038/s41563-023-01716-9

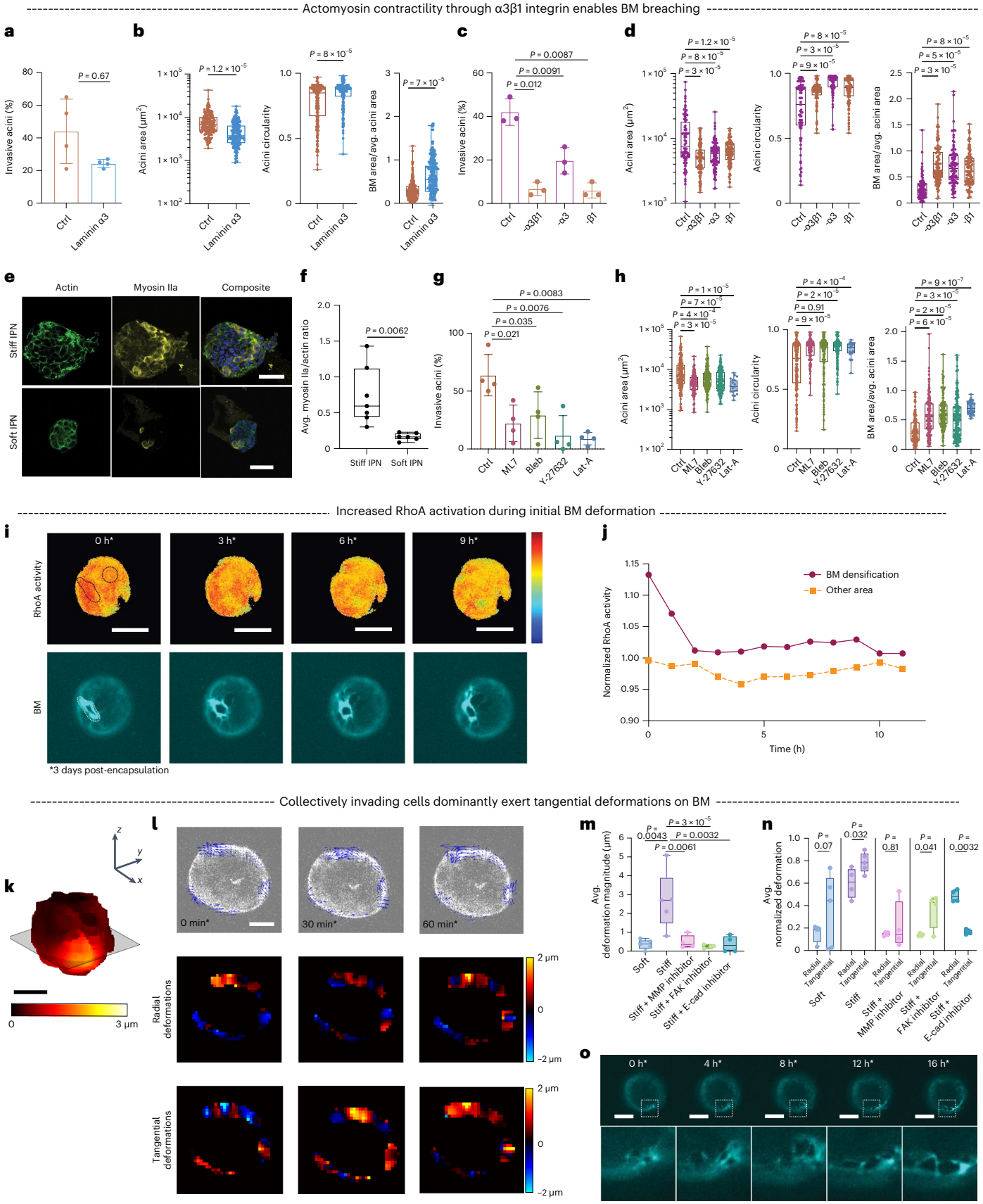

Laser ablation studies confirmed the presence of local deformations at the BM on ablating cell–BM interface (Extended Data Fig. 6, Supplementary Note 2 and Supplementary Videos 12 and 13). When normalized by the total deformation magnitude, tangential deformations in the BM were larger than radial deformations or indentations in the stiff invasive condition (Fig. 5l–n), suggesting that local cell contractility dominantly deforms the BM in the tangential direction. Blocking E-cadherin and inhibiting FAK and MMP in stiff IPNs significantly reduced the average

Fig. 5 | α3β1 integrin and actomyosin contractility enable BM breaching and collective invasion. a, Invasive acini percentage in stiff IPN control and with laminin antibody ($N = 4$ gels). **b**, Acini and BM metrics in stiff IPN control and with laminin antibody ($N \geq 30$ acini in four gels). **c**, Invasive acini percentage in stiff IPN control, and the control with α3, β1 and both α3 and β1 antibodies ($N = 3$ gels). **d**, Acini and BM metrics in stiff IPN control, and the control with α3, β1 and both α3 and β1 antibodies ($N \geq 30$ acini in three gels). **e**, Confocal images of actin (green), myosin IIa (yellow) and composite of actin, myosin IIa and nuclei (blue) in soft and stiff IPNs. **f**, Average myosin IIa/actin ratio in stiff and soft IPNs ($N \geq 6$ acini in three gels). **g**, Invasive acini percentage in stiff IPNs and with inhibitors ($N = 4$ gels). **h**, Acini and BM metrics in stiff IPNs and with inhibitors ($N \geq 20$ acini in four gels). **i**, RhoA FRET/donor ratio signal and BM signal over 9 h after encapsulation. Warmer colours correspond to higher RhoA activity. **j**, Normalized activity of RhoA at BM densification area (purple, solid) and other area (orange, dotted) divided by the average area intensity of an acini over 11 h. **k**, Representative heat map of the deformation magnitude of BM in three dimensions. **l**, Confocal images of BM overlaid with deformation vectors of the BM at different time points before invasion (top). Heat map of radial (middle) and tangential (bottom) deformations of the BM. **m**, Average deformation magnitude of BM in soft and stiff conditions, with inhibitors in stiff conditions ($N \geq 5$ acini in two gels). **n**, Average of normalized radial and tangential deformations in soft and stiff conditions, with inhibitors in stiff conditions ($N \geq 5$ acini in two gels). **o**, Representative time-lapse images of BM deformation showing tangential hole opening in the boxed square. Two-sided Welch's *t*-test used for the data in **a**, **b**, **f** and **n**. Brown–Forsythe and Welch ANOVA tests used for the data in **c**, **d**, **g**, **h** and **m**. Scale bars, 50 μm (**e**, **i**, **o**), 25 μm (**k**, **l**).

BM deformation magnitude compared with the control (Fig. 5m). Consistent with the observation of large tangential deformations of the BM in invasive conditions, BM tearing and hole dilation primarily occurred within the BM plane (Fig. 5o and Supplementary Video 14). In agreement with this, we observed differences in the collective motion of cells pre- and post-invasion in stiff IPNs compared with soft IPNs (Extended Data Fig. 7 and Supplementary Note 3). Overall, the deformation measurements of BM in various invasive and non-invasive conditions indicate that cells induce large tangential deformations in stiff invasive conditions to rupture the BM.

Theoretical modelling predicted local breaching in the BM

To examine how global cell volume expansion and tangential contractility could combine to drive BM breaching, we built a theoretical model that consisted of a growing tumour, surrounded by a thin BM and IPN matrix (Fig. 6a,b). Cells at the BM interface applied tangential contractile forces to the BM at either a baseline, resting or activated state (Fig. 6a,b). Next, we considered the independent roles of cell volume expansion and local cell contractility in inducing mechanical stresses onto the BM. Global cell volume expansion alone induced the pre-stretching of the BM, with higher tangential stresses on the BM relative to radial stresses (Fig. 6c,d). Local cell contractility alone, in the absence of global volume expansion, led to high tangential BM stresses in the region of the activated cell (Fig. 6e). Finally, when the global cell volume expansion was combined with activated local cell contractility, the highest tangential stresses in the BM were observed (Fig. 6f), which could potentially lead to BM breaching (Supplementary Note 4). Together, these data show that cell volume expansion synergistically acts with activated local cell contractility to drive BM rupture and facilitate invasion.

Hypotonic-induced cell volume expansion increased acini invasion in soft IPNs

Finally, we tested whether increased cell volumes in acini encapsulated in soft IPNs promoted invasion. Adding hypotonic media to acini encapsulated in soft IPNs increased the acini volume by approximately 40% relative to the control (Fig. 6g,h and Supplementary Video 15). There was increased invasion in hypotonic-treated acini, compared with the control, as qualitatively evident from BM breaching (Fig. 6i,j and Supplementary Videos 16 and 17). Quantitatively, we observed increased acini area, decreased acini circularity and decreased BM/average acini area (Fig. 6k). Moreover, the average magnitude of BM deformations became larger, and normalized tangential deformations were larger than normalized radial deformations in the hypotonic condition (Fig. 6l,m). Inhibiting ROCK or myosin contractility decreased the BM invasion and BM deformation (Fig. 6j–m and Supplementary Videos 18 and 19). Overall, these data support our proposed mechanism of cell volume expansion and local cell contractility combining to drive BM invasion.

Outlook

We developed an in vitro 3D model of breast carcinoma invasion to elucidate how protease-dependent and protease-independent modes of invasion contribute to the collective invasion of endogenous BM (Fig. 6k). Our 3D culture model recapitulated the key features of the physiological BM in DCIS, including the layering of laminin and collagen-IV, physiological thickness of the BM and the collective nature of invasion (Supplementary Note 5). In our model, acini became invasive in stiff IPNs and remained non-invasive in soft IPNs. Cells are likely able to sense IPN stiffness through the strong mechanical connectivity between endogenous BM and the IPN mediated by binding interactions between collagen-IV on the outer layer of endogenous BM with laminin and collagen-IV in the rBM in the IPN. We find that both protease and force-driven mechanisms were important in BM breaching, complementing previous work highlighting the role of proteases in individual tumour cell invasion[7,37,38], as well as forces in mediating protease-independent individual cell invasion of the BM[10,11]. However, cell structures that have been implicated in single-cell invasion and migration[9,39–41], including filopodia, invadopodia and lobopodia, were not observed during collective BM invasion; it is

Fig. 6 | Global cell volume expansion and localized contractility along the plane of the BM combine to rupture the BM. a, Schematic of force-driven BM breaching. Cell volume expansion induces growth stress (black curve), and cells exhibit baseline contractility (green line entitled "Resting"). At increased stiffness, some cells exhibit enhanced contractility (red line entitled "Exerting"). The IPN and BM are considered linear elastic (green and blue curves). **b**, Schematic showing normal BM, volume-expansion-induced tangential stress in the BM, local-contractility-induced tangential stress in the BM and BM breaching. **c**–**f**, Heat maps of tangential and radial stresses in the BM without volume expansion and contractility (**c**) and due to volume expansion (**d**), local contractility (**e**) and a combination of volume expansion and local cell contractility (**f**). The maximum stresses for each case are written on the heat map. **g**, Confocal images of laminin and F-actin in soft IPNs before and after treating with hypotonic media. The dashed circle (top right) corresponds to the laminin outline (top left). **h**, Bar plot of acini volume in control and hypotonic condition ($N \geq 5$ acini in two gels). **i**, Confocal images of laminin and F-actin in soft and hypotonic conditions. **j**, Percentage of invasive acini was the largest in hypotonic conditions ($N = 3$ gels). **k**, Acini area, circularity and BM area/average acini area in soft control, hypotonic and hypotonic with ROCK inhibition and blebbistatin conditions ($N \geq 8$ acini in three gels). **l**, Average deformation magnitude of BM in soft control, hypotonic and hypotonic with ROCK inhibition and blebbistatin conditions ($N \geq 6$ acini in three gels). **m**, Average of normalized radial and tangential deformations in soft control condition, hypotonic and hypotonic with ROCK inhibition and blebbistatin conditions ($N \geq 6$ acini in three gels). **n**, Schematic of protease-dependent and force-driven BM invasion by collective mammary epithelial cells. Protease activity combined with both cell volume expansion and tangential forces exerted by cells (either at cell–cell junctions or single-cell boundaries) locally on the BM enables breaching through the BM. Brown–Forsythe and Welch ANOVA tests were performed for the data in **j**–**l**. Two-sided unpaired *t*-tests were performed for the data in **h** and **m**. Scale bars, 25 μm (**g**, **i**).

https://doi.org/10.1038/s41563-023-01716-9

possible that these protrusions do not generate sufficient forces to invade the matrix beyond the BM in stiff, confining IPNs. Thus, cell–cell adhesions within the collective invasion in our model, mediated by E-cadherin and gap junctions, give rise to synergistic interactions and invasive behaviours that differ from single-cell migration and those driven by single-cell protrusions. Moreover, the inherent mechanics of cell migration during the initial BM breaching contrasted those in collagen-I in that collective BM invasion occurred at a single focal point

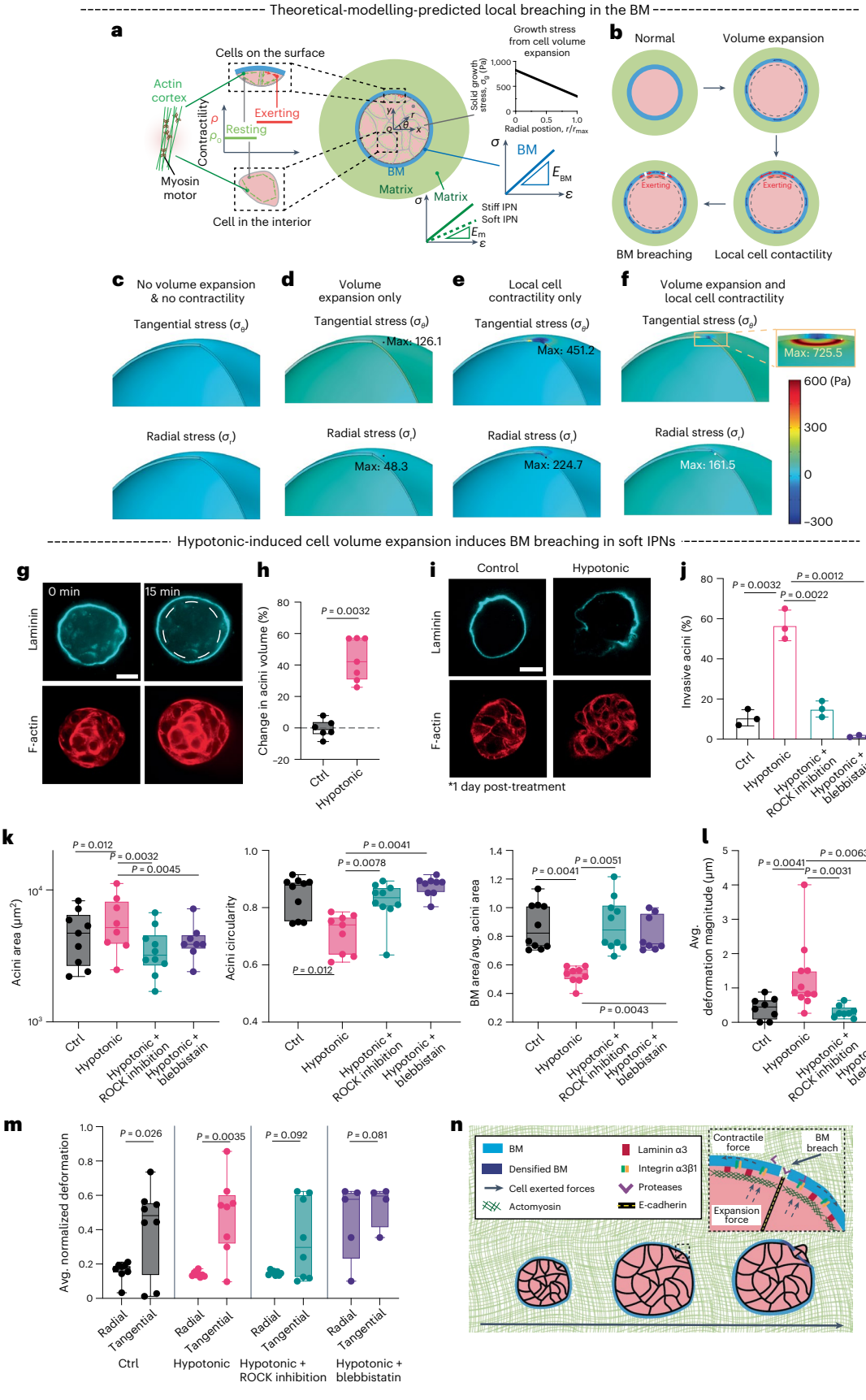

without single-cell detachment and did not involve K14-presenting leader cells (Extended Data Fig. 8)[42,43]. BM invasion was driven by a global increase in cell volumes, a collective phenomenon, and local cell contractile forces that act tangential to the BM, mediated by laminin α3 and α3β1 integrin interactions. These results indicate that therapeutics only targeting proteases may not be enough to inhibit the initial BM invasion; alternative therapeutic approaches could include inhibiting cellular contractility, limiting volume expansion and modulating BM mechanical properties to prevent cancer cell invasion. These insights into the initial invasion in breast cancer may extend to other carcinomas and diseases characterized by impaired BM function.

Online content

Any methods, additional references, Nature Portfolio reporting summaries, source data, extended data, supplementary information, acknowledgements, peer review information; details of author contributions and competing interests; and statements of data and code availability are available at https://doi.org/10.1038/s41563-023-01716-9.

References

1. Chaffer, C. L. & Weinberg, R. A. A perspective on cancer cell metastasis. *Science* **331**, 1559–1564 (2011).
2. Chang, J. & Chaudhuri, O. Beyond proteases: basement membrane mechanics and cancer invasion. *J. Cell Biol.* **218**, 2456–2469 (2019).
3. Yurchenco, P. D. Basement membranes: cell scaffoldings and signaling platforms. *Cold Spring Harbor Perspect. Biol.* **3**, a004911 (2011).
4. Virnig, B. A., Tuttle, T. M., Shamliyan, T. & Kane, R. L. Ductal carcinoma in situ of the breast: a systematic review of incidence, treatment, and outcomes. *J. Natl Cancer Inst.* **102**, 170–178 (2010).
5. Dillekås, H., Rogers, M. S. & Straume, O. Are 90% of deaths from cancer caused by metastases? *Cancer Med.* **8**, 5574 (2019).
6. Liotta, L. A. et al. Metastatic potential correlates with enzymatic degradation of basement membrane collagen. *Nature* **284**, 67–68 (1980).
7. Hotary, K., Li, X.-Y., Allen, E., Stevens, S. L. & Weiss, S. J. A cancer cell metalloprotease triad regulates the basement membrane transmigration program. *Genes Dev.* **20**, 2673–2686 (2006).
8. Eddy, R. J., Weidmann, M. D., Sharma, V. P. & Condeelis, J. S. Tumor cell invadopodia: invasive protrusions that orchestrate metastasis. *Cell* **27**, P595–607 (2017).
9. Wisdom, K. M. et al. Matrix mechanical plasticity regulates cancer cell migration through confining microenvironments. *Nat. Commun.* **9**, 4144 (2018).
10. Cáceres, R. et al. Forces drive basement membrane invasion in *Caenorhabditis elegans*. *Proc. Natl Acad. Sci. USA* **115**, 11537–11542 (2018).
11. Glentis, A. et al. Cancer-associated fibroblasts induce metalloprotease-independent cancer cell invasion of the basement membrane. *Nat. Commun.* **8**, 924 (2017).
12. Chaudhuri, O., Cooper-White, J., Janmey, P. A., Mooney, D. J. & Shenoy, V. B. Effects of extracellular matrix viscoelasticity on cellular behaviour. *Nature* **584**, 535–546 (2020).
13. Clark, A. G. & Vignjevic, D. M. Modes of cancer cell invasion and the role of the microenvironment. *Curr. Opin. Cell Biol.* **36**, 13–22 (2015).
14. Padmanaban, V. et al. E-cadherin is required for metastasis in multiple models of breast cancer. *Nature* **573**, 439–444 (2019).
15. Kai, F. B., Drain, A. P. & Weaver, V. M. The extracellular matrix modulates the metastatic journey. *Dev. Cell* **49**, 332–346 (2019).
16. Reuten, R. et al. Basement membrane stiffness determines metastases formation. *Nat. Mater.* **20**, 892–903 (2021).
17. Gkretsi, V. & Stylianopoulos, T. Cell adhesion and matrix stiffness: coordinating cancer cell invasion and metastasis. *Front. Oncol.* **8**, 145 (2018).
18. Chaudhuri, O. et al. Extracellular matrix stiffness and composition jointly regulate the induction of malignant phenotypes in mammary epithelium. *Nat. Mater.* **13**, 970–978 (2014).
19. Acerbi, I. et al. Human breast cancer invasion and aggression correlates with ECM stiffening and immune cell infiltration. *Integr. Biol.* **7**, 1120–1134 (2015).
20. Sinkus, R. et al. Imaging anisotropic and viscous properties of breast tissue by magnetic resonance-elastography. *Magn. Reson. Med.* **53**, 372–387 (2005).
21. Stowers, R. S. et al. Extracellular matrix stiffening induces a malignant phenotypic transition in breast epithelial cells. *Cell. Mol. Bioeng.* **10**, 114–123 (2017).
22. Wolf, K. et al. Compensation mechanism in tumor cell migration: mesenchymal-amoeboid transition after blocking of pericellular proteolysis. *J. Cell Biol.* **160**, 267–277 (2003).
23. Hagbard, L. et al. Developing defined substrates for stem cell culture and differentiation. *Phil. Trans. R. Soc. B* **373**, 20170230 (2018).
24. Tilghman, R. W. & Parsons, J. T. Focal adhesion kinase as a regulator of cell tension in the progression of cancer. *Semin. Cancer Biol.* **18**, 45–52 (2008).
25. Chang, J., Pang, E. M., Adebowale, K., Wisdom, K. M. & Chaudhuri, O. Increased stiffness inhibits invadopodia formation and cell migration in 3D. *Biophys. J.* **119**, 726–736 (2020).
26. Murphy, D. A. & Courtneidge, S. A. The 'ins' and 'outs' of podosomes and invadopodia: characteristics, formation and function. *Nat. Rev. Mol. Cell Biol.* **12**, 413–426 (2011).
27. Lee, H., Gu, L., Mooney, D. J., Levenston, M. E. & Chaudhuri, O. Mechanical confinement regulates cartilage matrix formation by chondrocytes. *Nat. Mater.* **16**, 1243–1251 (2017).
28. Lee, H., Stowers, R. & Chaudhuri, O. Volume expansion and TRPV4 activation regulate stem cell fate in three-dimensional microenvironments. *Nat. Commun.* **10**, 529 (2019).
29. Guo, M. et al. Cell volume change through water efflux impacts cell stiffness and stem cell fate. *Proc. Natl Acad. Sci. USA* **114**, E8618–E8627 (2017).
30. Han, Y. L. et al. Cell swelling, softening and invasion in a three-dimensional breast cancer model. *Nat. Phys.* **16**, 101–108 (2019).
31. Becker, D., Blase, C., Bereiter-Hahn, J. & Jendrach, M. TRPV4 exhibits a functional role in cell-volume regulation. *J. Cell Sci.* **118**, 2435–2440 (2005).
32. McEvoy, E., Han, Y. L., Guo, M. & Shenoy, V. B. Gap junctions amplify spatial variations in cell volume in proliferating tumor spheroids. *Nat. Commun.* **11**, 6148 (2020).
33. Bazzoun, D. et al. Connexin 43 maintains tissue polarity and regulates mitotic spindle orientation in the breast epithelium. *J. Cell Sci.* **132**, jcs223313 (2019).
34. Khalil, A. A. et al. Collective invasion induced by an autocrine purinergic loop through connexin-43 hemichannels. *J. Cell Biol.* **219**, e201911120 (2020).
35. Carter, W. G., Kaur, P., Gil, S. G., Gahr, P. J. & Wayner, E. A. Distinct functions for integrins alpha 3 beta 1 in focal adhesions and alpha 6 beta 4/bullous pemphigoid antigen in a new stable anchoring contact (SAC) of keratinocytes: relation to hemidesmosomes. *J. Cell Biol.* **111**, 3141–3154 (1990).
36. Pertz, O., Hodgson, L., Klemke, R. L. & Hahn, K. M. Spatiotemporal dynamics of RhoA activity in migrating cells. *Nature* **440**, 1069–1072 (2006).
37. Kessenbrock, K., Plaks, V. & Werb, Z. Matrix metalloproteinases: regulators of the tumor microenvironment. *Cell* **141**, 52–67 (2010).
38. Jacob, A. & Prekeris, R. The regulation of MMP targeting to invadopodia during cancer metastasis. *Front. Cell Dev. Biol.* **3**, 4 (2015).
39. Arjonen, A., Kaukonen, R. & Ivaska, J. Filopodia and adhesion in cancer cell motility. *Cell Adhes. Migr.* **5**, 421–430 (2011).

40. Eschenbruch, J. et al. From microspikes to stress fibers: actin remodeling in breast acini drives myosin II-mediated basement membrane invasion. *Cells* **10**, 1979 (2021).
41. Gaiko-Shcherbak, A. et al. Cell force-driven basement membrane disruption fuels EGF- and stiffness-induced invasive cell dissemination from benign breast gland acini. *Int. J. Mol. Sci.* **22**, 3962 (2021).
42. Ilina, O. et al. Cell–cell adhesion and 3D matrix confinement determine jamming transitions in breast cancer invasion. *Nat. Cell Biol.* **22**, 1103–1115 (2020).
43. Cheung, K. J., Gabrielson, E., Werb, Z. & Ewald, A. J. Collective invasion in breast cancer requires a conserved basal epithelial program. *Cell* **155**, 1639–1651 (2013).

Methods

Cell culture

MCF10A human mammary epithelial cells (ATCC) were cultured in Dulbecco's modified Eagle's medium/Nutrient Mixture F-12 (DMEM/F12) medium (Thermo Fisher) supplemented with 5% horse serum (Thermo Fisher), 20 ng ml^{-1} EGF (Peprotech), 0.5 µg ml^{-1} hydrocortisone (Sigma), 100 ng ml^{-1} cholera toxin (Sigma), 10.0 µg ml^{-1} insulin (Sigma) and 1% penicillin/streptomycin (Thermo Fisher). MCF10A cells expressing RFP-LifeAct were used for live-imaging experiments. MDA-MB-231 human breast cancer adenocarcinoma cells (ATCC) and HEK293T human embryonic kidney cells (ATCC) were cultured in high-glucose DMEM (Thermo Fisher) supplemented with 10% foetal bovine serum (Hyclone) and 1% penicillin/streptomycin. MCF10AT and MCF10CA1a cells, a gift from L. Wakefield (NIH), were cultured in MCF10A medium for experimental consistency. Cells were routinely split every 3–4 days with 0.05% trypsin/ethylenediaminetetraacetic acid (EDTA) and cultured in a standard humidified incubator at 37 °C and 5.00% CO_2.

Tissue immunohistochemistry

Immunofluorescence (IF) staining was performed on paraffin-embedded tissue microarray sections (Stanford TA 417, 419 and 424). Primary antibodies used for IHC staining include laminin-332 (Santa Cruz Biotech catalogue no. sc-28330) and E-cadherin (BD Pharmingen catalogue no. 560062 conjugated with af647). Tissue microarray sections measuring 4 µm were deparaffinized in three changes of xylene for 10 min each and hydrated in a gradient series of ethyl alcohol. For E-cadherin, a target retrieval in 10 mM citrate pH6 (Agilent, catalogue no. S2369) was performed to retrieve the antigenic sites at 116 °C for 3 min. For laminin-332, retrieval was done with proteinase K (Agilent, catalogue no. S3020) for 15 min at room temperature and visualized with anti-mouse IgG1k af647 (Invitrogen/Life Technologies, catalogue no. A21240). All the samples were counterstained with 4′,6-diamidino-2-phenylindole (DAPI) (Invitrogen/Life Technologies, catalogue no. P36935)

Alginate preparation

High-molecular-weight sodium alginate rich in guluronic acid blocks (FMC Biopolymer, Protanal LF 20/40, high molecular weight, 280.0 kDa) was dialysed against deionized water for 3–4 days using dialysis tubing with a molecular-weight cutoff of 3.5 kDa. Alginate was subsequently treated with activated charcoal, sterile filtered and lyophilized. Before experiments, lyophilized alginate was reconstituted to 2.5 wt% in serum-free DMEM/F12 (Thermo Fisher).

Acini formation

Six-well plates were coated with 150 µl of rBM (Corning) in six-well plates were placed into a 37 °C incubator with CO_2 to gel for at least 10 min. To form MCF10A acini in the six-well plates, MCF10A cells were trypsinized, strained through a 40 µm cell strainer to enrich for single cells, counted on a Vi-CELL (Beckman Coulter Life Sciences) and seeded at a final concentration of 1×10^5 cells ml^{-1} hydrogel. Cells were cultured in 2 ml of complete DMEM/F12 medium supplemented with 2% rBM. The addition of 2% rBM is necessary to drive the development from single cells to acini[44]. rBM-supplemented complete media were replenished on day 4. Once the acini were formed, the acini were extracted by adding 2 ml of ice-cold 50 mM EDTA in phosphate-buffered saline (PBS) per well and scrapping off the layers with a cell scraper. After a 20 min incubation on ice, the acini-containing EDTA mixture was spun down for 5 min at 500×*g* at 4 °C. The acini were resuspended in MCF10A resuspension media and centrifuged at 500×*g* for another 5 min. After centrifugation, the supernatant was aspirated, and the acini were resuspended in DMEM/F12 media.

For live-imaging experiments of BM, except FRET, Alexa Fluor 488-conjugated anti-laminin-5 antibody, clone D4B5 (Millipore Sigma) was added to the resuspended media at a 1:100 concentration and incubated on ice for 1 h. For pharmacological inhibition experiments, inhibitors were added to the resuspended media and incubated on ice for 1 h. After incubation, the cells were spun down for 5 min at 500×*g* at 4 °C, the supernatant was aspirated and the acini were resuspended in DMEM/F12 media.

Encapsulation of acini in hydrogels

To form IPNs, 24-well plates were coated with 50 µl rBM (Corning) and allowed to gel for at least 10 min in a 37 °C incubator with CO_2 (ref. 18). Standard 24-well plates (Corning) were used for immunohistochemistry and 24-well glass-bottom plates (Cellvis) were used in the experiments that required sample imaging. Alginate was mixed with rBM, acini and DMEM/F12 in a 1.5 ml Eppendorf tube and added to a 1.0 ml Luer-Lok syringe (Cole-Parmer). An appropriate volume of each component was added to reach a concentration of 5.0 mg ml^{-1} alginate and 4.4 mg ml^{-1} rBM in the final IPNs. For experiments requiring fiducial marker beads, 0.2 µm dark-red microspheres (Thermo Fisher) were added to a syringe containing alginate at a 100-fold dilution. The second 1 ml syringe contained DMEM/F12 containing 5 mM $CaSO_4$ for soft IPNs or DMEM/F12 containing 20 mM $CaSO_4$ for stiff IPNs. The two syringes were coupled with a female–female Luer-Lok (Cole-Parmer), quickly mixed and instantly deposited into the 24-well plate coated with rBM. A transwell insert (Millipore) was immediately placed on top of the IPN to prevent floating and the IPNs containing acini were placed in a 37 °C incubator with CO_2 to gel for at least 30 min. After the IPNs have gelled, 1.5 ml of complete media, with pharmacological inhibitors, if required, was added.

Acini and cell volume measurements

Imaris Bitplane (version 9.9.0) was used to create surface renderings of RFP-LifeAct-transfected MCF10A cells. Images acquired during confocal imaging were imported into Imaris (Bitplane), a software that enables 3D volume rendering and analysis. Cell volume measurements were made using the RFP channel of the cells. For cell volume, the Cells program was used with the following parameters: smallest cell diameter, 10.00 µm; cell membrane detail, 2.00 µm; cell filter type, local contrast. For cell nuclei, the Surfaces program was used with the following parameters: surface grain size, 0.800 µm; diameter of the largest sphere, 5.000 µm. All the images were manually filtered for abnormal cell or nuclei volumes.

Mechanical testing

Material stiffness and plasticity measurements were performed using an AR2000EX stress-controlled rheometer (TA Instruments) with 25 mm top- and bottom-plate stainless steel geometries. IPN solutions without cells were deposited onto the centre of the bottom plate. A 25 mm flat-top plate was quickly lowered to form a 25 mm disc before gelation of the IPN and mineral oil (Sigma-Aldrich) was applied to the edge of the IPN to prevent sample dehydration. A time sweep was conducted at 37 °C, 1 rad s^{-1} and 1% strain for 2 h, and the measurements were taken once the storage modulus reached equilibrium. Young's modulus (E) was calculated as follows:

$$E = 2G^* \times (1 + \upsilon), \tag{1}$$

where Poisson's ratio υ is assumed to be 0.5 and G^* is the bulk modulus calculated from the storage (G') and loss moduli (G'') measured as

$$G^* = (G'^2 + G''^2)^{1/2}. \tag{2}$$

To characterize plasticity, a creep recovery test was performed immediately after the time sweep. Strain measurements were recorded as the IPNs were subjected to a constant shear stress (25 Pa) for 1 h, followed by a recovery period where the sample was unloaded (0 Pa). The resulting strain was recorded as a function of time after 10,000 s.

IF for fixed cells

To fix hydrogel samples for IF staining, hydrogels containing wild-type MCF10A cells were fixed for 30 min in warmed 4% paraformaldehyde in serum-free DMEM/F12 at room temperature. Gels containing acini were washed twice in PBS for 15 min, incubated in 30% sucrose solution in PBS overnight and incubated in a 1:1 mixture of 30% sucrose and optimal-cutting-temperature compound (Tissue-Tek) for at least 4 h. The gels were embedded in optimal-cutting-temperature compound and frozen on dry ice. Frozen gels were sectioned with a cryostat into ~50 µm sections and adhered onto microscope slides. Slides were blocked in a solution of 10.0% goat serum (Thermo Fisher), 1.0% bovine serum albumin (Sigma), 0.1% Triton X-100 (Sigma) and 0.3 M glycine (Sigma) for 1 h at room temperature. Primary antibodies were diluted in the blocking solution (1:100) and incubated at 4 °C overnight. Alexa Fluor 488–phalloidin (1:100 dilution, Thermo Fisher) and DAPI (1 µg ml^{-1}) were diluted in the blocking solution and incubated for 1 h. Fluorescently conjugated secondary antibodies were incubated in a blocking solution for 1 h at room temperature. The slides were then washed three times for 5 min in Dulbecco's phosphate-buffered saline, and coverslips were applied with Prolong Gold antifade reagent (Thermo Fisher). The slides were imaged on a Leica SP8 laser-scanning confocal microscope with a ×63 1.40-numerical-aperture (NA) Plan Apo oil-immersion objective.

Antibodies used were anti-laminin-5 (γ2 chain, clone D4B5, Millipore Sigma, #MAB19562, 1:500), anti-collagen-IV antibody (Sigma, #SAB4500369, 1:500), anti-non-muscle myosin IIa antibody (Abcam, #ab55456, 1:100), anti-phospho-FAK antibody (Tyr397, Invitrogen, #700255, 1:500), anti-E-cadherin (BD Biosciences, #610181, 1:100), anti-β4 integrin (Thermo Fisher. 1:500), Alexa Fluor 488 goat anti-mouse IgG_{2a} (#A21131, 1:1,000), Alex Fluor 488 goat anti-mouse IgG_{2b} (#A21141, 1:1,000), Alexa Fluor 647 goat anti-mouse IgG_1 (#A21240, 1:1,000) and Alexa Fluor 647 goat anti-rabbit (#A21244, 1:1,000).

For collagen-IV and laminin-332 staining of the endogenous BM, the acini were not embedded in a hydrogel since collagen-IV is also present in rBM. Instead, seven-day acini were seeded onto poly-lysine coverslips, fixed by adding 1 ml formaldehyde for 20 min at room temperature, and washed twice with PBS.

Pharmacological inhibition

Pharmacological inhibitors were added to the cell media after the hydrogels were formed. Images were acquired three days later. The concentrations of pharmacological inhibitors used were as follows: 50.0 µM blebbistatin (Abcam, myosin II inhibitor), 10.0 µM FAK inhibitor (Selleck Chem), 25.0 µM GM6001 (Millipore, MMP inhibitor), 30.0 µM GSK205 (Calbiochem, TRPV4 antagonist), 2.5 µM latrunculin A (Tocris Bioscience, actin polymerization inhibitor), 100.0 µM marimastat (Tocris, MMP inhibitor), 25.0 µM ML-7 (Tocris, myosin light chain kinase inhibitor), 500.0 µM carbenoxolone (Sigma, gap junction inhibitor) and 25.0 µM Y-27632 (Sigma, ROCK inhibitor). The protease inhibitor cocktail contained 20.0 µM marimastat, 20.0 µM pepstatin A (Sigma), 20.0 µM E-64 (Sigma), 0.7 µM aprotinin (Sigma) and 2.0 µM leupeptin (Sigma)[22]. Note that the concentration of marimastat in the protease cocktail is lower than the concentration of the marimastat inhibitor alone.

The concentrations of function-blocking antibodies used were as follows: 1 µg ml^{-1} anti-laminin 5 antibody (R&D Systems, #MAB2144); 1 µg ml^{-1} α3 anti-integrin antibody, clone P1B5 (Sigma, #MAB1952Z); 1 µg ml^{-1} β1 anti-integrin antibody, clone P5D2 (Abcam, #ab24693); 1 µg ml^{-1} α6 anti-integrin antibody, clone GoH3 (Sigma, #MAB1378); 1 µg ml^{-1} β4 anti-integrin antibody, clone ASC-8 (Sigma, #MAB2059); and 1 µg ml^{-1} E-cadherin antibody, clone DECMA-1 (Sigma, #MABT26). Appropriate controls used include IgG from mouse serum (Sigma, #I5381) and IgG from rat serum (Sigma, #I4131).

Confocal microscopy

Microscopy imaging was performed with a laser-scanning Leica SP8 confocal microscope or a Nikon Ti2-E inverted microscope, both fitted with a temperature and incubator control suitable for live imaging (37 °C, 5% CO_2). A ×10 0.45-NA dry objective or 20× 0.75-NA dry objective was used for the Nikon microscope. A 10× 0.4-NA dry objective was used for the Leica microscope. For live-cell time-lapse imaging, the images were acquired three days after acini were encapsulated in IPNs; images were acquired overnight every 30, 60 or 120 min. For pharmacological inhibition experiments, images were acquired three days after acini were encapsulated in IPNs.

BM breaching and cell invasion quantification

Invasive acini and their BM structures were manually counted in at least ten fields of view with at least 40 total acini counted in three experiments. Images with 100 and 10 µm stack sizes were acquired. Invasive acini were identified as those in which the collective cells were identified to have migrated from the acini in a two-dimensional field of view. The maximum intensity projection was taken for each 100 µm image stack and a Gaussian blur image filter was applied using ImageJ (version 2.9.0). Next, a threshold was applied to the images to convert the image from greyscale into a binary image. Further quantification of BM breaching and cell invasion parameters were performed. These metrics include (1) acini circularity, (2) projected area of acini in the plane of invasion (acini area) and (3) ratio of BM-enclosed area to acini area (BM area/average acini area) in the plane of invasion. Acini circularity indicates the breaking of acini symmetry as the invasion occurs; the acini area quantifies the extent of cells invading into the ECM, and BM area/average acini area quantifies the extent of cells invading through the BM, in which a smaller ratio indicates greater invasion through the BM. The combination of low acini circularity and large acini area are characteristics of invading acini. A BM area/average acini area close to 1 is characteristic of intact BM that has not been breached, whereas a BM area/average acini area less than 1 is characteristic of BM that has been breached.

Osmotic pressure studies

To modulate the osmotic pressure in the culture media, 400 Da PEG 400 (TCI America) was added[28]. PEG 400 concentrations of 0% wt/vol (0 mOsm l^{-1}), 2% wt/vol (50 mOsm l^{-1}) and 4% wt/vol (100 mOsm l^{-1}) was added to the media after hydrogel formation.

FRET experiments

An optimized biosensor for RhoA was developed based on a single-chain, genetically encoded FRET biosensor design[36]. The original, dimeric ECFP and dimeric citrine YFP fluorescent proteins were exchanged for the monomeric versions containing the A206K mutation[45]. The mECFP was further modified using synonymous codons to prevent random homologous recombination during stable genomic integration and expression in target cells[46]. The biosensor was further optimized to improve the dynamic range of FRET change by utilizing a circularly permutated 173 mECFP (Extended Data Fig. 9a). The mcp173ECFP was produced by a two-step PCR reaction using the following primer sets: 5′-GCTAATGCATATACAAGGATCCGGCATGGATGGAAGCGTGCAGCTGGCTGATC-3′, 5′-GGTTAATACATGTTAGAAGCTTTCAATATTATGCCTAATTTTAAAG-3′, 5′-TTGGACACCATGCCGCCGCTGCCGCCTTTATACAGTTCATCCATTCCCA-3′ and 5′-ACTGTATAAAGGCGGCAGCGGCGGCATGGTGTCCAAAGGAGAAGAACTGTT-3′. The combination of the monomeric mutations and circular permutations resulted in approximately 4.5-fold improvement in the fluorometric response in FRET/donor ratio comparing the constitutively activated mutant Q63L ('on') versus the dominant negative T19N ('off') versions in live suspensions of HEK293T cells overexpressing the biosensor and measured using a spectrofluorometer (Extended Data Fig. 9b). The improvement in the dynamic range was achieved by

an increased on-state FRET due to the optimized dipole coupling from the use of a circularly permutated mECFP as well as an improvement in the fall-off of FRET during the off state from the monomerization of the fluorescent proteins (Extended Data Fig. 9c). The biosensor appropriately responded to various mutations as demonstrated previously for the original version of this biosensor[36], as well as interaction with an upstream regulator Rho-guanine nucleotide dissociation inhibitor (Extended Data Fig. 9d). Transient expression of the constitutively activated Q61L versus the dominant negative T19N versions of the biosensor in MCF10A cells showed approximately 40% difference in the average whole-cell FRET/donor ratio in microscopy, whereas the relative ratio differences as measured within single cells indicated a local dynamic range of 1.0 to 3.4 in the pseudocolour scaling (Extended Data Fig. 9e). The as-designed biosensor does not compete against binding to other cellular targets of activated RhoA, which minimizes the overexpression artefacts in living cells (Extended Data Fig. 9f).

The parental MCF10A cells were stably transduced with tetracycline-OFF-transactivator system (tet-OFF, Clontech)[47]. The biosensor expression cassette was transduced into the stable tet-OFF MCF10A cell line under the regulation of a tet-inducible minimal CMV promoter (pRetro-X-Puro, Clontech) and selected using puromycin for a stably integrated population. The biosensor expression was subsequently induced by withholding doxycycline for 48 h, and the cells were sorted using fluorescence-activated cell sorting to enrich for the population of positive transductants. Biosensor expression levels on induction in the sorted population were analysed by western blot, showing approximately 38% of the levels of the endogenous RhoA GTPase (Extended Data Fig. 10a,b). The induction of the biosensor expression in MCF10A cells did not affect the relative expression levels of endogenous Rho GTPases, including RhoA, Rac1 and Cdc42 (Extended Data Fig. 10c–h).

MCF10A cells stably harbouring the inducible RhoA biosensor were normally maintained in the MCF10A growth media with 1 μg ml^{-1} doxycycline, 1 mg ml^{-1} G418 and 10 μg ml^{-1} puromycin. Also, 48 h before the encapsulation of cells in IPNs, MCF10A with RhoA biosensors were trypsinized and plated in tissue culture plates without doxycycline. This process was repeated 24 h before encapsulation into the IPNs. The cells were then encapsulated into IPNs without doxycycline. The cells were imaged with a Nikon spinning-disc confocal microscope under ×20 0.75-NA objective with 445 nm laser excitation and the emission filters 511/20 nm for donor FRET (cyan) and 534/30 nm for acceptor FRET, with 2 × 2 binning of the Hamamatsu ORCA-Flash4.0 scientific complementary metal–oxide–semiconductor camera at 1 s exposure time per image. The *Z* stacks were taken every 20 min in the donor and acceptor channels of the FRET biosensor, together with Alexa Fluor 647-conjugated laminin antibody to label the BM.

Post-processing of biosensor FRET images utilized ratiometric biosensor analysis, which consisted of flat-field correction, background subtraction, image registration and ratio calculations[48]. Flat-field correction was performed based on the acquisition of a set of *Z* stacks of shading images that consisted of cell-free fields of view with identical exposure and field illumination as the biosensor image sets. The donor and acceptor FRET images were divided by the shading images to achieve flat-field correction. A small region of interest in the cell-free background area was selected in the flat-field-corrected image sets, and the mean grey value from such a region of interest was subtracted from the whole field of view at each time point at each *Z* position to obtain the background-subtracted image sets. The resulting background-subtracted *Z* stacks of images were segmented by producing and applying binary masks using manual histogram thresholding. The segmented acceptor-FRET channel image stacks were then divided by the segmented donor image stacks to produce the ratio data stacks, followed by the application of a linear pseudocolour lookup table to depict the relative differences in FRET/donor ratio and the corresponding RhoA activity in cells.

Western blotting

Cells were lysed on ice for 30 min in a buffer containing 1% NP-40, 50 mM Tris (pH 7.4), 150 mM NaCl, 10 mM EDTA, 1 mM Pefabloc SC (Sigma) and protease inhibitor cocktail (Sigma). The lysate was clarified by centrifugation at 22,000 g for 15 min at 4 °C. The lysates were resolved by 10–12% sodium dodecyl sulfate–polyacrylamide gel electrophoresis. Proteins were transferred to polyvinylidene fluoride membranes. After blocking for at least 1 h in 5% bovine serum albumin in Tris-buffered saline containing 1% Tween-20 (TBS-T), the membranes were incubated with primary antibodies at 1:500 dilution overnight at 4 °C. The membranes were incubated with secondary fluorescently labelled antibodies (LI-COR Biosciences) at 1:20,000 dilution for 1 h at room temperature. Immunoblots were visualized using the Odyssey Imager (LI-COR Biosciences).

GST-RBD pull-down experiments

HEK293T cells were plated overnight at a density of 0.9×10^6 cells on poly-L-lysine-coated six-well plates. The mVenus-RhoA Q63L and T19N mutants and the RhoA biosensor containing Q63L mutation, and that which additionally contained a p21-binding domain from the p21-activated kinase 1, were transfected using the polyethyleneimine reagent at 2 μg DNA to 8 μl polyethyleneimine ratio for each well. After 24 h, the cells were lysed in a buffer containing 1% NP-40, 50 mM Tris HCl (pH 7.4), 500 mM NaCl, 10 mM $MgCl_2$, 1 mM phenylmethylsulfonyl fluoride and a protease inhibitor cocktail (Sigma-Aldrich). The lysates were clarified by centrifugation at 22,000 g for 15 min at 4 °C. Biosensor pull-downs were performed using purified Rhotekin-RBD-agarose beads[49]. To prepare the glutathione-agarose beads, 72 mg of glutathione-agarose (Sigma-Aldrich) was suspended in 10 ml sterile water and incubated at 4 °C for 1 h. The suspension was centrifuged at 1,200 g for 30 s at 4 °C, and the pellet was washed three times with sterile water, followed by washing two times in a resuspension buffer containing 50 mM Tris (pH 8.0), 40 mM EDTA and 25% sucrose. To generate GST-Rhotekin-RBD, pGEX-RBD (a gift from G. Bokoch) was transformed into BL21(DE3)-competent strain of bacteria (Agilent Technologies) and propagated in a shaker incubator at 225 r.p.m. and 37 °C until an optical density of 0.9 at 600 nm was reached. Then, 0.2 mM isopropyl β-D-1-thiogalactopyranoside was added to induce the protein synthesis, at 225 r.p.m. and 24 °C overnight. Following an overnight incubation, the bacteria were pelleted and resuspended in 20 ml of the resuspension buffer containing 1 mM phenylmethylsulfonyl fluoride, protease inhibitor cocktail (Sigma-Aldrich) and 2 mM β-mercaptoethanol, and rotated for 20 min at 4 °C. Following the incubation, 8 ml of the detergent buffer (50 mM Tris (pH 8.0), 100 mM $MgCl_2$ and 0.2% wt/vol Triton X-100) was added, and the mixture was incubated at 4 °C for 10 min on a rotator. Ultrasonication was used to disrupt the cell membrane (4× cycles of 30 s ultrasonication followed by 1 min rest on ice) and centrifuged at 22,000 g for 45 min at 4 °C. Then, 1 ml of the hydrated and washed glutathione-agarose beads were added to the clarified supernatant and incubated at 4 °C for 1 h on a rotator. The beads were pelleted by centrifugation at 1,200 g for 30 s and washed four times with the wash buffer containing 50 mM Tris (pH 7.6), 50 mM NaCl and 5 mM $MgCl_2$, followed by resuspension in 500 μl of 50:50 glycerol/wash buffer. Cell lysates were incubated with Rhotekin-RBD-conjugated agarose beads for 1 h at 4 °C on a rotator, washed 3× in the lysis buffer, resuspended in the final sample buffer, boiled at 99 °C for 5 min and analysed by western blotting.

Antibodies for western blotting

EGFP (Roche, 11814460001, clones 7.1 and 13.1; mixture mouse monoclonal), Rac1 (Cytoskeleton, ARC03; mouse monoclonal), Cdc42 (Santa Cruz Biotechnology, sc-8401, clone B-8; mouse monoclonal), RhoA (Santa Cruz Biotechnology, sc-418, Clone 26C4; mouse monoclonal) and β-actin (Santa Cruz Biotechnology, sc-69879, clone AC-15; mouse monoclonal) were used. Unless otherwise stated, all primary antibodies were used at 1:500 dilution for western blots.

Quantifying BM deformations before invasion

To quantify BM deformations in three dimensions, we employed fast-iterative digital volume correlation[50] with a subset size of 32 × 32 × 16 voxels and spacing of 4 voxels in MATLAB R2022a. To quantify the BM deformations in the plane of invasion before invasion, we performed fast-iterative digital image correlation (FIDIC)[50] with a subset size of 16 × 16 and spacing of 4 pixels (~2.0–2.8 μm) on confocal images of the BM before invasion. For each invasive acini, the time and confocal image of BM at which the invasion occurred was identified. At this invasive plane, the confocal images of the BM corresponding to at least 30 min and at most 4 h before the invasion were considered, and FIDIC was performed between two consecutive time-lapse images. To avoid deformations with noisy correlations from FIDIC, we only considered deformations with correlation coefficients above 0.2 (which is at least an order of magnitude greater than the correlation coefficient of noise). To measure the radial and tangential deformations in the BM, we transformed into polar coordinates using the centre of the BM as the origin.

Laser ablation

Laser ablation was performed on a multiphoton laser-scanning confocal microscope (Zeiss LSM 780) with a ×25/0.8-NA oil-immersion objective and under cell culture conditions (37 °C, 5% CO_2) at the Stanford Cell Sciences Imaging Facility. A micro-point laser at 405 nm was used to ablate the cell–cell and cell–BM edges in an acini using a single pulse of 100% laser power (maximum power, 1.85 mW). To measure recoil or retraction in acini after ablation, we employed digital image correlation to measure the deformations between two consecutive time-lapse images.

Modelling and finite element simulation

For a tumour spheroid, we adopted the multiplicative decomposition of the deformation gradient $\mathbf{F}$ into an elastic tensor $\mathbf{F}_e$ and a growth tensor $\mathbf{F}_g$, such that $\mathbf{F} = \mathbf{F}_e\mathbf{F}_g$. The growth tensor can be expressed by $\mathbf{F}_g = \lambda_g\mathbf{I}$, where λ_g is the growth stretch and $\mathbf{I}$ is the second-order identity tensor. With this definition of the growth tensor, we can then determine the elastic component of the deformation gradient as $\mathbf{F}_e = \mathbf{F}\mathbf{F}_g^{-1}$. The mechanical behaviour of the tumour spheroid may then be described by a neo-Hookean hyperelastic formulation, with a Cauchy stress given by

$$\boldsymbol{\sigma} = \bar{p}_0\mathbf{I} + \frac{G}{J_e}\left(\mathbf{B}_e - \frac{1}{3}\mathrm{tr}\,(\mathbf{C}_e)\,\mathbf{I}\right) + K(J_e - 1)\,\mathbf{I}, \tag{3}$$

where $\bar{p}_0$ is the contractility of actomyosin; J_e is the determinant of the elastic component of the deformation gradient; $\mathbf{B}_e = J_e^{-\frac{2}{3}}\mathbf{F}_e\mathbf{F}_e^{\mathrm{T}}$ and $\mathbf{C}_e = J_e^{-\frac{2}{3}}\mathbf{F}_e^{\mathrm{T}}\mathbf{F}_e$ are the left and right Cauchy–Green tensors, respectively; G is the material shear modulus; and K is the material bulk modulus. In our simulations, the BM and hydrogel matrix are linear elastic. Although the BM is known to be nonlinear elastic, and the IPNs are viscoelastic and viscoplastic, this simplification should not impact the fundamental physics of this problem. We solve our system using COMSOL Multiphysics (version 6.0) to simulate the stress field in the BM; the results are shown in Fig. 6j.

Statistical analysis and reproducibility

Measurements were performed on 2–3 biological replicates from separate experiments. Sample size (N) and statistical tests performed for each figure are indicated in the respective figure legends. Data were handled in Microsoft Excel (version 16.14). Statistical analyses were performed using GraphPad Prism (version 9.1.0 for Mac laptop; https://www.graphpad.com/). In the bar plots, the top line of the box represents the mean and the error bar represents the standard deviation, unless otherwise noted, and the individual data points are simultaneously represented. In the box plots, boxes represent the interquartile range, and the centre of the boxes represent the median. The whiskers represent the maximum and minimum values.

Reporting summary

Further information on research design is available in the Nature Portfolio Reporting Summary linked to this article.

Data availability

Raw images are available from the corresponding author upon request due to the large file sizes of images. Source data are provided with this paper.

Code availability

The code for the theoretical model is available via GitHub at https://github.com/edwinnewton/Collective-invasion-of-the-basement-membrane-in-breast-cancer.

References

44. Debnath, J., Muthuswamy, S. K. & Brugge, J. S. Morphogenesis and oncogenesis of MCF-10A mammary epithelial acini grown in three-dimensional basement membrane cultures. *Methods* **30**, 256–268 (2003).
45. Von Stetten, D., Noirclerc-Savoye, M., Goedhart, J., Gadella, T. W. J. & Royant, A. Structure of a fluorescent protein from *Aequorea victoria* bearing the obligate-monomer mutation A206K. *Acta Cryst.* **F68**, 878–882 (2012).
46. Wu, B. et al. Synonymous modification results in high-fidelity gene expression of repetitive protein and nucleotide sequences. *Genes Dev.* **29**, 876–886 (2015).
47. Miskolci, V., Hodgson, L. & Cox, D. Using fluorescence resonance energy transfer-based biosensors to probe Rho GTPase activation during phagocytosis. *Methods Mol. Biol.* **1519**, 125–143 (2017).
48. Spiering, D., Bravo-Cordero, J. J., Moshfegh, Y., Miskolci, V. & Hodgson, L. Quantitative ratiometric imaging of FRET-biosensors in living cells. *Methods Cell. Biol.* **114**, 593–609 (2013).
49. Jennings, R. T. & Knaus, U. G. Rho family and Rap GTPase activation assays. *Methods Mol. Biol.* **1124**, 79–88 (2014).
50. Bar-Kochba, E., Toyjanova, J., Andrews, E., Kim, K. S. & Franck, C. A fast iterative digital volume correlation algorithm for large deformations. *Exp. Mech.* **55**, 261–274 (2015).

Acknowledgements

We gratefully acknowledge an Advancing Science in America (ARCS) fellowship for J.C., a National Defense Science and Engineering Graduate fellowship for J.C., a National Science Foundation Graduate Research fellowship for J.C., a National Institutes of Health National Cancer Institute Grant (R37 CA214136) to O.C. and a National Institute of General Medicine Grant (R35 GM136226) to L.H. L.H. is an Irma T. Hirschl Career Scientist. The computational work was supported by National Cancer Institute awards U54CA261694 (to Z.S. and V.S.); National Institute of Biomedical Imaging and Bioengineering awards R01EB017753 (to V.S.) and R01EB030876 (to V.S.); NSF Center for Engineering Mechanobiology Grant CMMI-154857 (to Z.S. and V.S.); and NSF Grant DMS-1953572 (to V.S.). The funding from the Office of Research and Development in the Palo Alto VA Medical Center pays the salary for M.P.M. We thank J. Notbohm (The University of Wisconsin-Madison) for providing the MATLAB program to compute the curvature of the BM.

Author contributions

Conceived and designed the experiments: J.C., A.S. and O.C. Performed the experiments: J.C., A.S., S.V., C.S., N.H.K.A., D.I., R.S., K.L. and L.H. Contributed to the analytical guidance: A.S., S.S., L.H. and M.P.M. Designed and implemented the computational model: Z.S. and V.S. Supervised and administered the project: M.C.B., R.B.W. and O.C. Acquired the funding: O.C. Wrote the manuscript: J.C., A.S., Z.S., S.V., V.S. and O.C.

Competing interests
The authors declare no competing interests.

Additional information
Extended data is available for this paper at https://doi.org/10.1038/s41563-023-01716-9.

Supplementary information The online version contains supplementary material available at https://doi.org/10.1038/s41563-023-01716-9.

Correspondence and requests for materials should be addressed to Ovijit Chaudhuri.

Peer review information *Nature Materials* thanks Konstantinos Konstantopoulos, Paolo Provenzano and the other, anonymous, reviewer(s) for their contribution to the peer review of this work.

https://doi.org/10.1038/s41563-023-01716-9

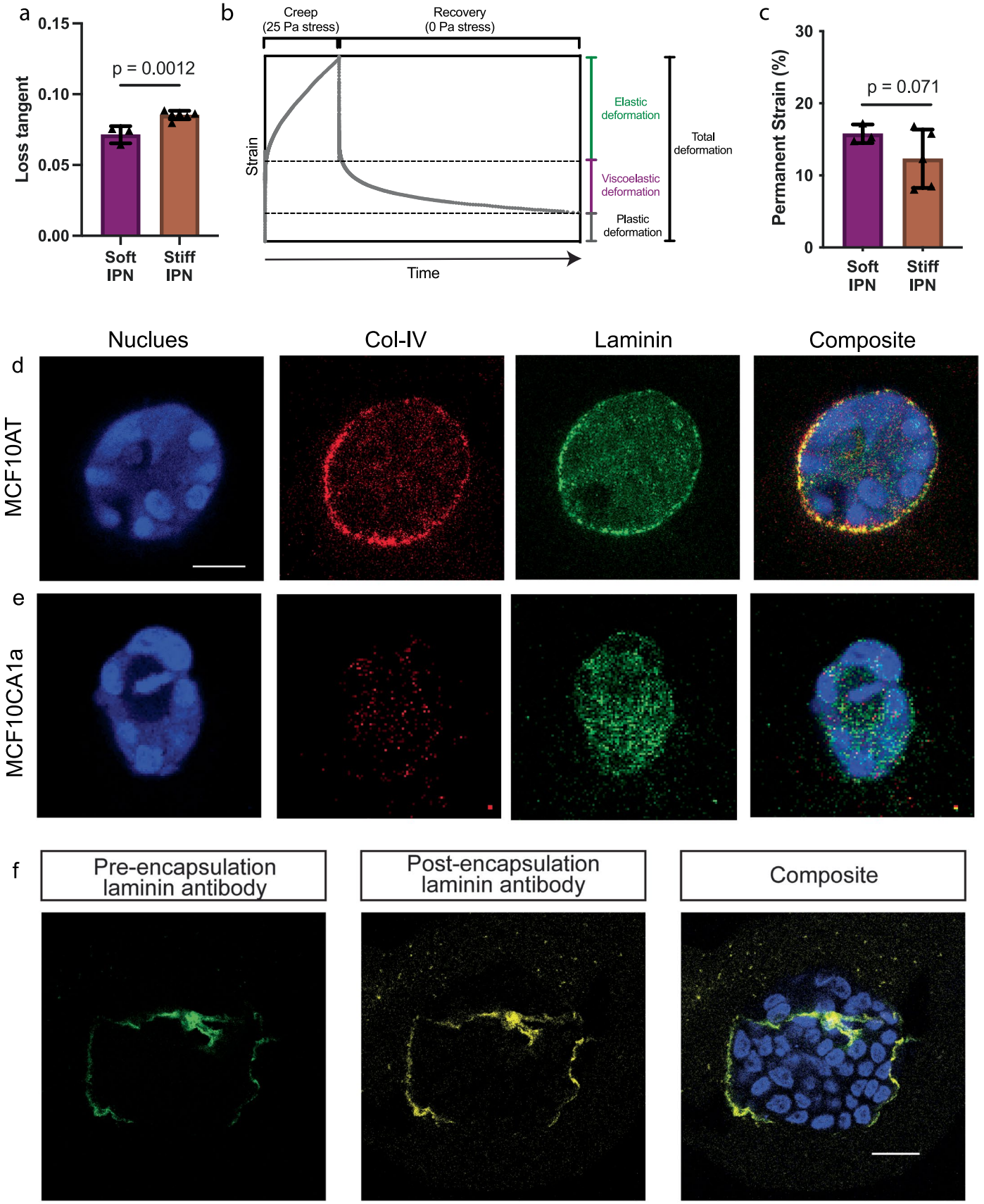

Extended Data Fig. 1 | See next page for caption.

https://doi.org/10.1038/s41563-023-01716-9

Extended Data Fig. 1 | Loss tangent and permanent strain of soft and stiff IPNs, basement membrane in transformed cells and after encapsulation of MCF10A cells into IPNs. a, Loss tangent of alginate-rBM IPNs (soft and stiff) (N = 3–6 gels). **b**, Representative creep and recovery test. Example creep and recovery test used to measure plasticity, in which plasticity is quantified as the remaining strain after 10,000 seconds divided by the total deformation during the creep test. **c**, Permanent strain of alginate-rBM IPNs (soft and stiff) (N = 3–6 gels). **d-e**, Confocal images of nuclei, collagen-IV, and laminin of MCF10AT (d) and MCF10CA1a acini (e). **f**, No additional laminin secretion observed in BM after encapsulation of acini into IPNs. Laminin-antibody added to MCF10A acini before IPN encapsulation (green) and laminin-antibody added after IPN encapsulation (yellow) show no new secretion of laminin within 24 hours. Two-sided unpaired t-test was performed for panels (**a**) and (**c**). Scale bars, 25 μm (**d**, **e**), 20 μm (**f**).

https://doi.org/10.1038/s41563-023-01716-9

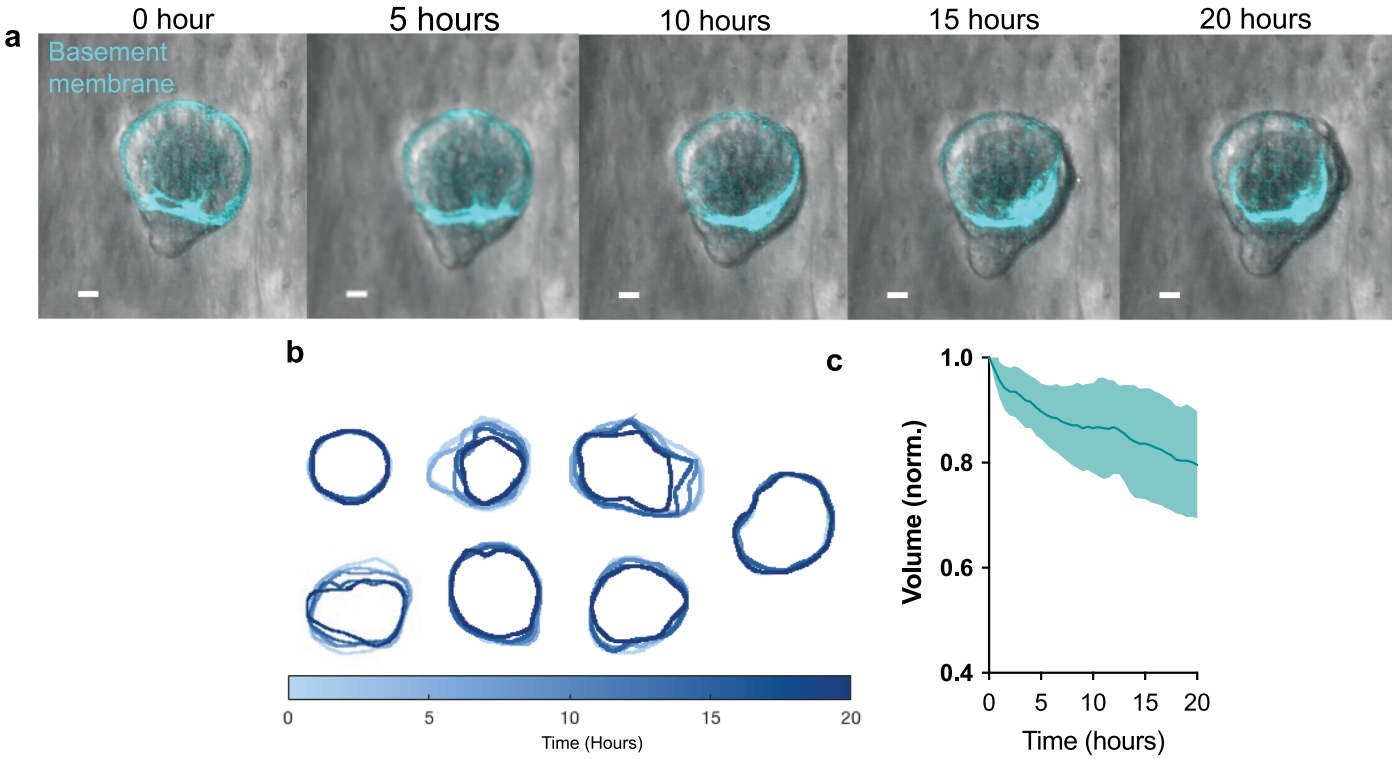

Extended Data Fig. 2 | Analysis of BM volume after the breaching. a a, Time-lapse of cell invasion (brightfield) and BM (cyan) movement. **b**, Time-lapse outlines of BM over twenty hours. **c**, Normalized volumes of BM shells over twenty hours. Scale bars, 20 μm (**a**).

https://doi.org/10.1038/s41563-023-01716-9

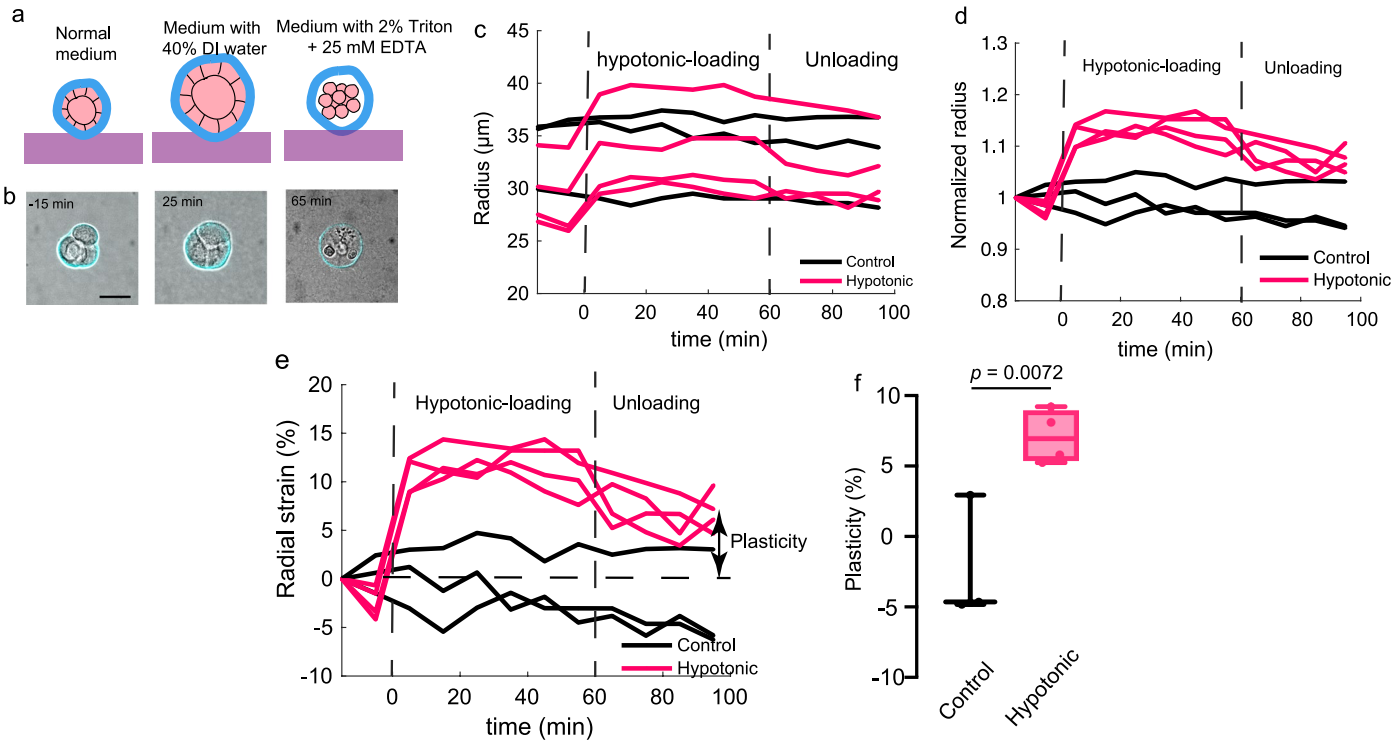

Extended Data Fig. 3 | Measurement of BM plasticity through hypotonic loading. a, Schematic of an acini in normal media (left), hypotonic media (middle), and triton-EDTA solution following treatment in hypotonic media (right) seeded on rBM. **b**, Overlay of confocal images of BM (cyan) and the corresponding phase image of acini in normal media (left), hypotonic media (middle), and triton-EDTA solution (right). **c**, Radii of acini in reference, hypotonic-loading, and unloading conditions of control and hypotonic-treated acini (N = > 3 acini). **d**, Normalized radii of acini in reference, hypotonic-loading, and unloading conditions of control and hypotonic-treated acini (N = > 3 acini). **e**, Radial strain in reference, hypotonic-loading, and unloading conditions of control and hypotonic-treated acini (N = > 3 acini). **f**, Mechanical plasticity (or residual radial strain) of acini in soft IPN with control and hypotonic media (N = > 3 acini). Two-sided Welch's t-test was performed for panel (**a**). Scale bar, 25 μm (**a**).

https://doi.org/10.1038/s41563-023-01716-9

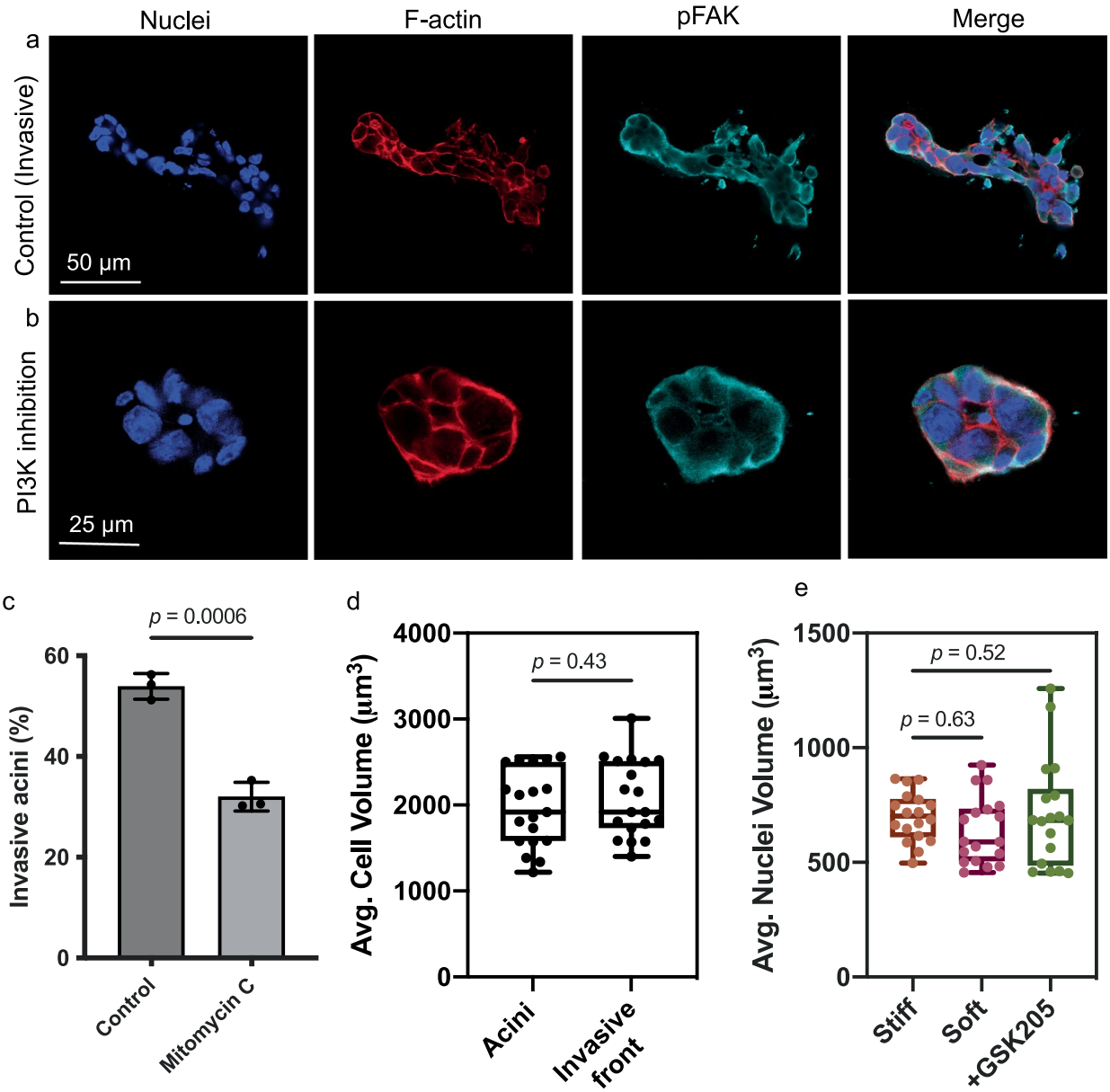

Extended Data Fig. 4 | Role of proliferation in invasion, and measure of cell and nuclei volumes. a, Confocal images of nuclei, F-actin, pFAK and merged images of acini in stiff IPN with control. **b**, Confocal images of nuclei, F-actin, pFAK and merged images of acini in stiff IPN with PI3K inhibitor. **c**, Percentage of invasive acini in stiff IPNs with and without inhibition of proliferation by mitomycin C (N = 3 gels). **d**, Cell volume in invasive front and acini of invasive acini. No differences in average cell volume between cells in invasive front and cells within the acini of invasive acini in stiff IPNs (N => 30 acini in 3 gels). **e**, Measurement of nuclei volume in stiff, soft, and stiff + GSK205 conditions. No differences in nuclei volume between soft, stiff, and GSK205 treated stiff IPNs (N => 30 acini in 3 gels). Two-sided Unpaired t-test was performed for panels (**c**) and (**d**). One-way ANOVA was performed for panel (**e**). Scale bar, 50 µm (**a**), 25 µm (**b**).

https://doi.org/10.1038/s41563-023-01716-9

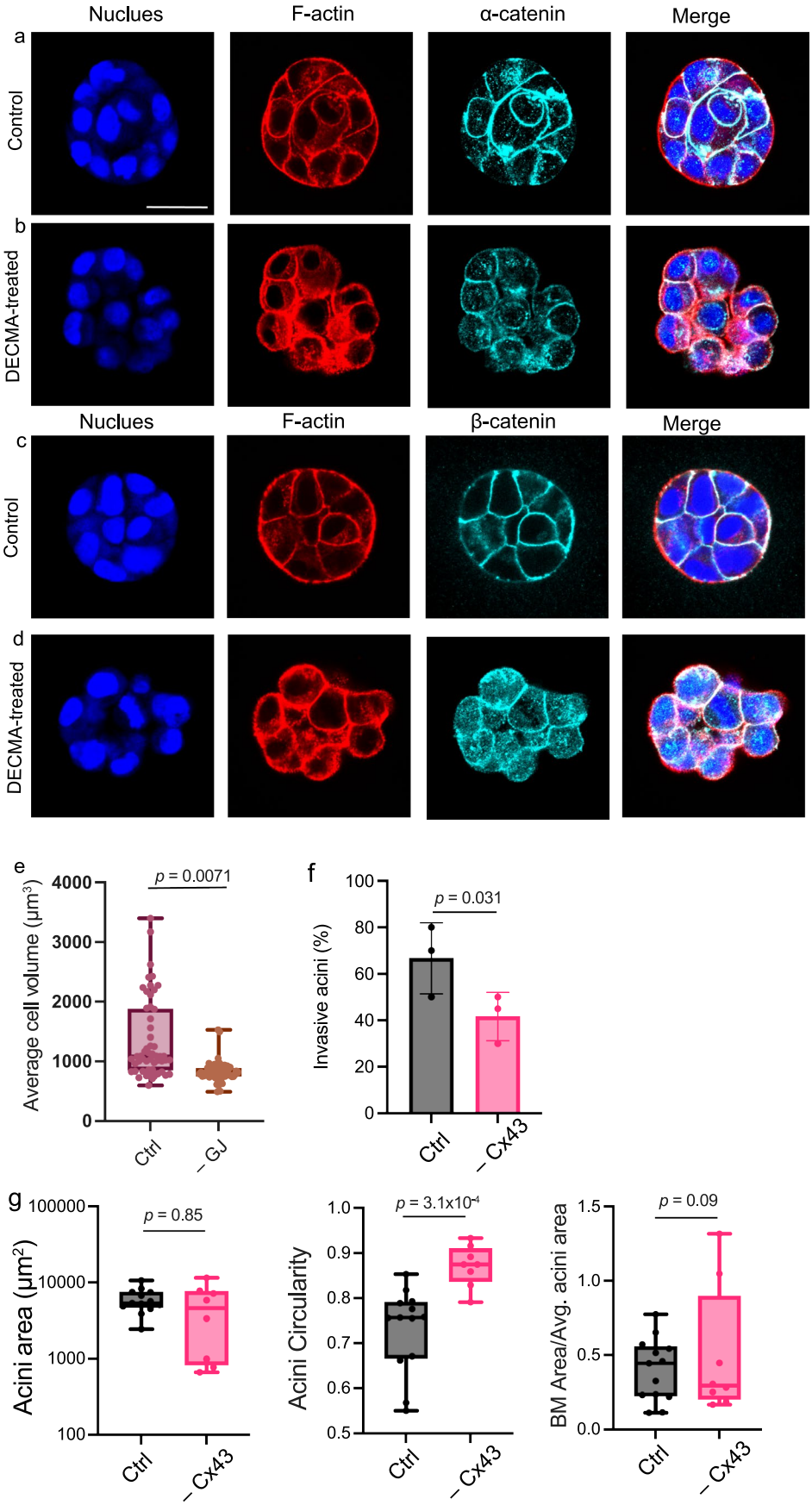

Extended Data Fig. 5 | See next page for caption.

https://doi.org/10.1038/s41563-023-01716-9

Extended Data Fig. 5 | E-cadherin blocking, gap junction inhibition and Cx43 KO. a, **b**, Confocal images of nuclei, F-actin, and α-catenin, and corresponding merges under control, and DECMA-treated conditions encapsulated in stiff IPNs on Day 1. **c**, **d**, Confocal images of nuclei, F-actin, and β-catenin, and the corresponding merge under control, and DECMA-treated conditions encapsulated in stiff IPNs on Day 1. **e**, Average cell volume was decreased when treated with gap junction inhibitor compared to control (N = > 30 acini in 3 gels). **f**, Percentage of invasion was significantly higher in control compared to Cx43 KO cells (N = 3 gels). **g**, Acini area were similar in control and Cx43 KO conditions. Acini of Cx43 KO cells were more circular compared to the control condition. BM area to average acini area were similar in control and Cx43 KO conditions (N = > 6 acini in 3 gels). Two-sided Welch's t-tests were performed for panels (**e**), (**f**), and (**g**). Scale bar, 25 μm (**a**-**d**).

https://doi.org/10.1038/s41563-023-01716-9

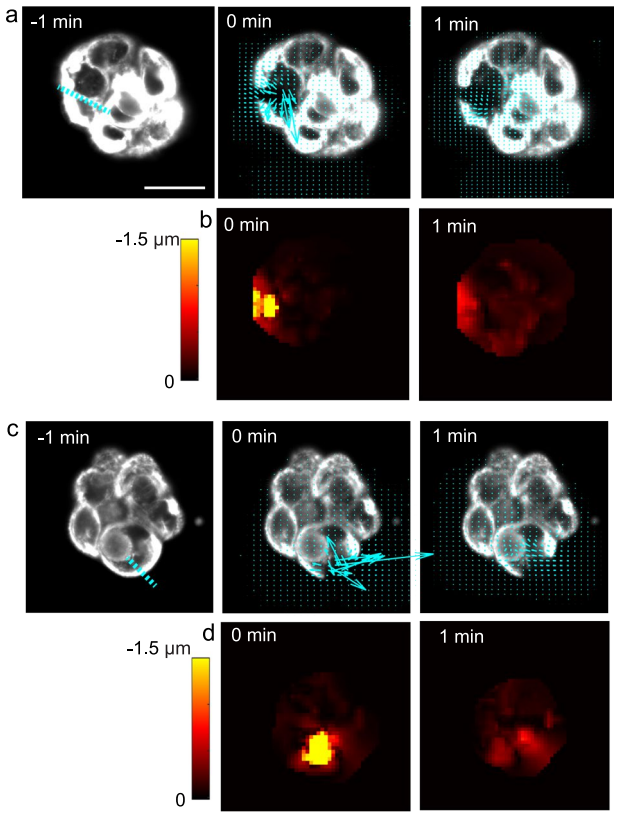

Extended Data Fig. 6 | Laser ablation of cell-cell and cell-BM interfaces in acini. a, c, Confocal images of F-actin at −1, 0, and 1 min where 0 min correspond to right after laser ablation of cell-cell (a; left; highlighted by the dotted line) and cell-BM edge (c; left; highlighted by the dotted line). Deformation vectors from laser ablation were overlaid on the confocal images of the F-actin in middle and right panels. **b, d**, Deformation magnitude in the plane of laser ablation right after the ablation of cell-cell (b) and cell-BM edges (d). Scale bar, 25 µm.

https://doi.org/10.1038/s41563-023-01716-9

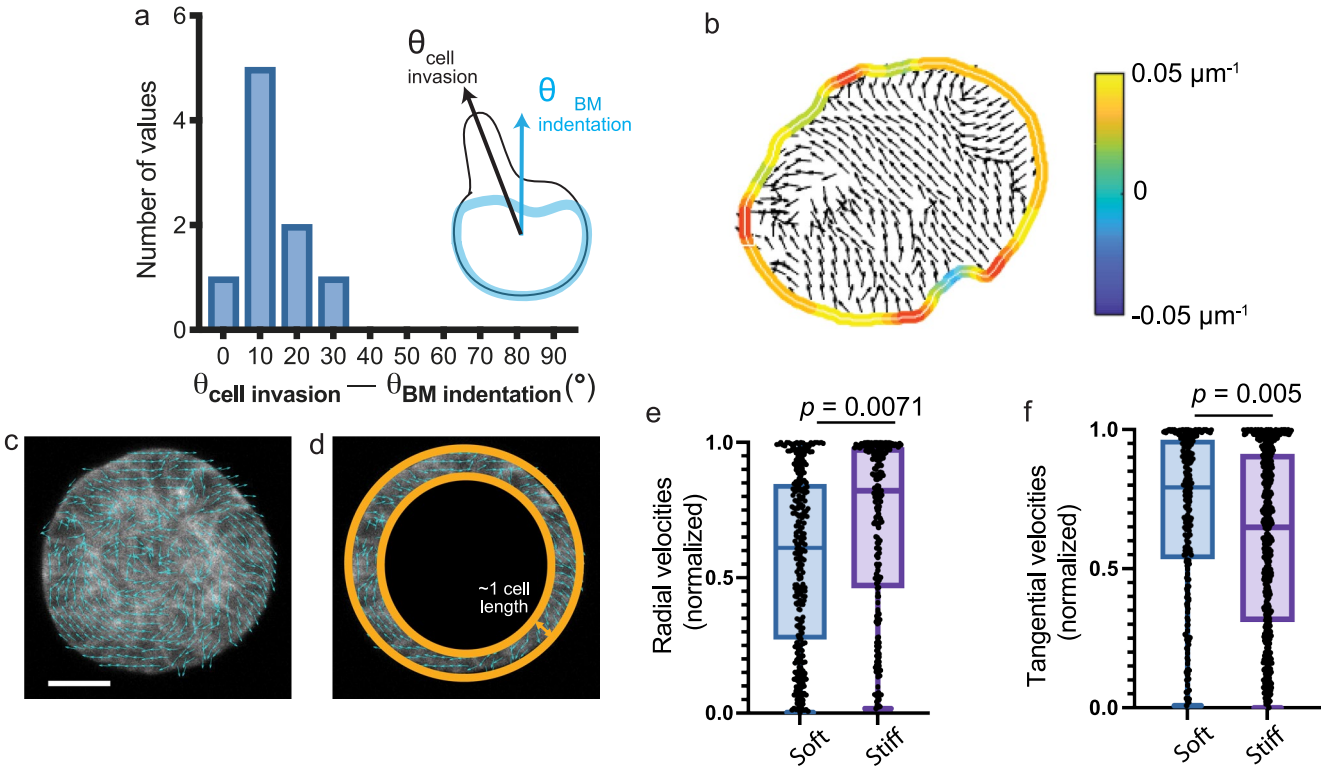

Extended Data Fig. 7 | Analysis of collective invasion, BM curvature, and collective motion of cells. a, Histogram of differences between the angle between cell invasion and laminin indentation (N = 10 acini in 3–6 gels). **b**, Representative image of direction of cell movement within the acini compared to BM curvature. Arrow in points to area of BM deformation. **c**, Acini actin with cell velocity vectors shown in cyan. **d**, Schematic of region analyzed for cell velocity measurements. **e-f**, Tangential cell velocities and radial cell velocities, normalized by the total velocity, in acini with intact BM and breached BM (N = > 30 acini in 3 gels). Two-sided unpaired t-test was performed for panels (**e**) and (**f**). Scale bar, 25 μm (**c**).

https://doi.org/10.1038/s41563-023-01716-9

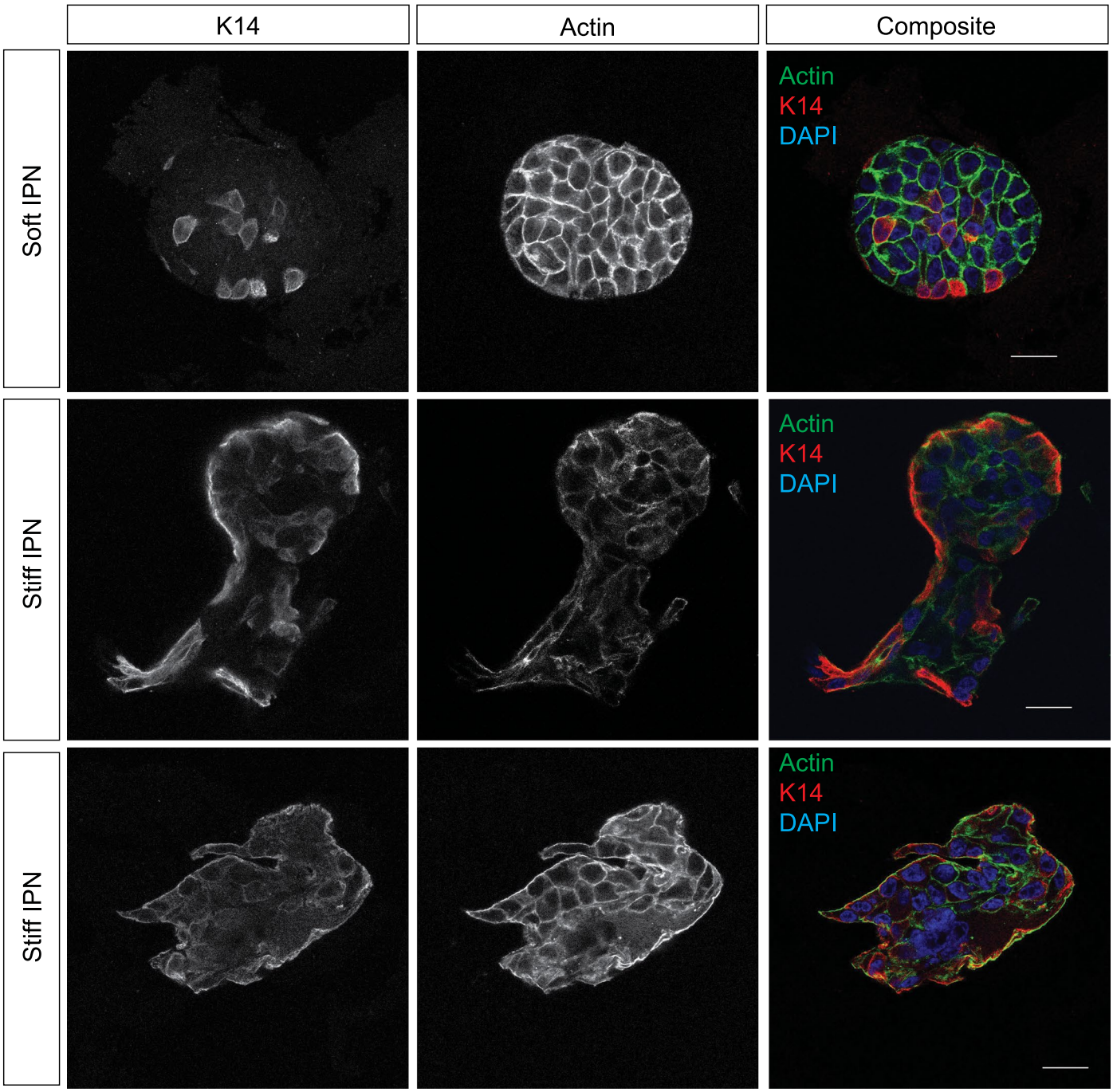

Extended Data Fig. 8 | Heterogeneous K14 staining for cells in invasive clusters. Cytokeratin-14 (red), actin (green) and DAPI (blue) staining in acini of soft and stiff IPNs. Scale bar, 25 μm.

https://doi.org/10.1038/s41563-023-01716-9

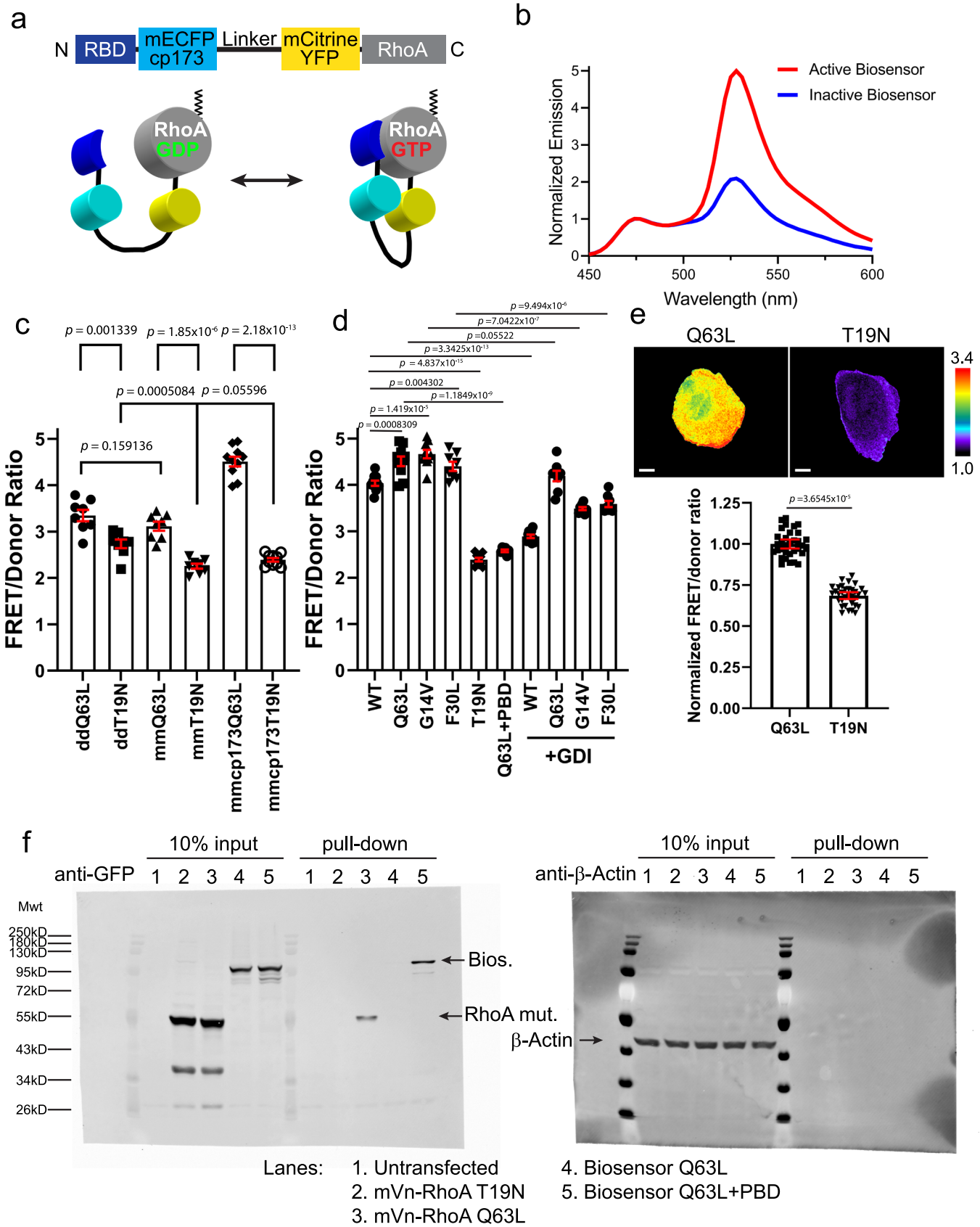

Extended Data Fig. 9 | See next page for caption.

https://doi.org/10.1038/s41563-023-01716-9

Extended Data Fig. 9 | Optimized FRET biosensor for RhoA GTPase. a, Schematic representation of the optimized, single-chain, genetically-encoded FRET biosensor for RhoA GTPase, based on the previously published design[36]. Fluorescent proteins are replaced with monomeric versions containing the A206K mutations, and the dipole coupling angle is optimized by using a circular permutation of the donor at position 173. **b**, Representative, normalized fluorescence emission spectra are shown, from the constitutively activated Q63L ('Active Biosensor') and the dominant negative T19N ('Inactive Biosensor') mutant versions of the biosensors overexpressed in live cell suspensions of HEK293T cells, excited at 433 nm and the emission scanned from 450 nm to 600 nm. Spectra are normalized to the emission maxima of the donor fluorophore at 427 nm. **c**, Changes in FRET/donor ratio responses comparing active versus inactive mutant versions of the RhoA biosensor during optimization of the fluorescent protein FRET pair. 'dd' indicates original RhoA biosensor[36] containing the dimerizing A206 residue in both the donor and the acceptor fluorescent proteins, 'mm' indicates A206K monomeric mutations are introduced into the original ECFP and the Citrine YFP, and 'mmcp173' indicates A206K monomeric mutations in both the donor and acceptor fluorescent proteins in addition to circular permutation of the donor at amino acid position 173 (N = 7 experiments for dd and mm, and N = 10 for mmcp173), shown with SEM. **d**, Fluorometric FRET/donor emission ratio of the optimized RhoA biosensor overexpressed in HEK293T cells. WT biosensor expression and the Q63L, G14V, and F30L constitutively activated mutant biosensors showed high emission ratios. The dominant negative T19N mutant biosensor, constitutively activated (Q63L) biosensor with non-specific binding domain (PBD) showed low emission ratios. 2-fold excess expression of the guanine nucleotide dissociation inhibitor-1 (GDI) showed reduced ratio for those that are targeted by GDI, whereas the Q63L mutant that does not bind GDI produced elevated ratio (N = 10 experiments for WT, Q63L and T19N, N = 9 for G14V, N = 8 for F30L, and all +GDI conditions, N = 6 for Q63L+PBD); all shown with SEM. **e**, Ratiometric microscopy measurements of the transiently expressed RhoA biosensor mutants in MCF10A cells under 60x magnification, and the quantification of the whole-cell average ratio values. White bars = 10 µm. Linear pseudocolor corresponds to the indicated scaling limits (N = 3 experiments); shown with 95% confidence intervals of the aggregate data points from the pooled datapoints. **f**, Competitive pull-downs of the optimized RhoA biosensor. Lane designations are also shown. The Q63L constitutively activated RhoA biosensor is pulled down by excess exogenous GST-RBD, only when the built-in RBD domain of the biosensor is exchanged for a non-Rho-specific PBD. Two-sided Student's t-test was performed for panels (**c**), (**d**) and (**e**).

https://doi.org/10.1038/s41563-023-01716-9

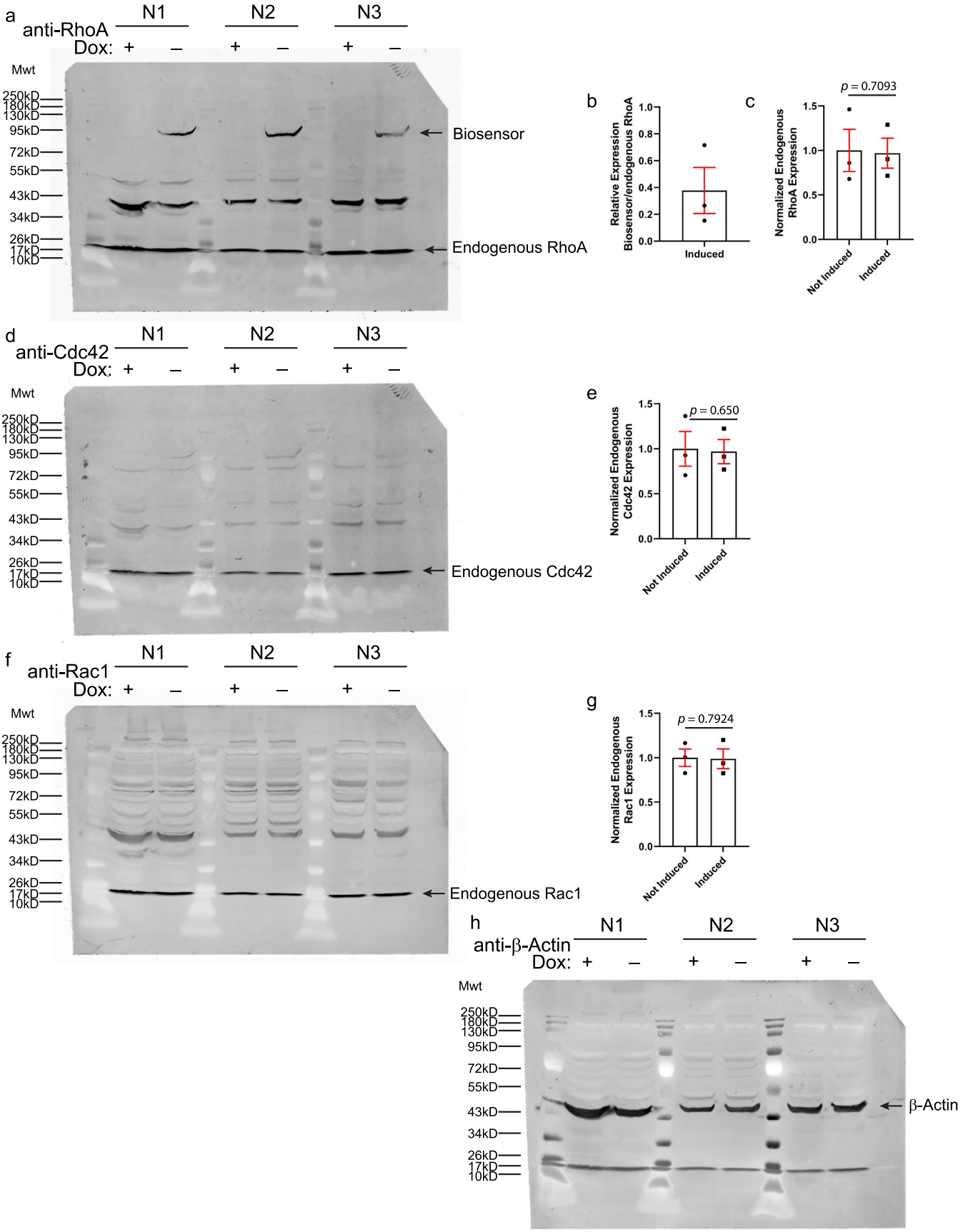

Extended Data Fig. 10 | See next page for caption.

https://doi.org/10.1038/s41563-023-01716-9

Extended Data Fig. 10 | Biosensor expression analysis in MCF10A cells. **a**, Inducible expression of the optimized RhoA biosensor in MCF10A cells, stably incorporating the biosensor under the tetracycline-OFF regulation. MCF10A cells stably transduced with the tet-OFF inducible biosensor expression system were FACS sorted to enrich for the biosensor-positive cell population and analyzed following the same biosensor induction protocol used in the current biological assays. **b**, Quantification of induced RhoA biosensor band intensities compared to the endogenous RhoA, indicating 37.8% +/−17.2% of the endogenous RhoA levels, shown with SEM, N = 3 experiments. **c**, Quantification of (**a**); induced expression of the RhoA biosensor does not affect the relative expression levels of endogenous RhoA (N = 3 experiments). **d**, Western blot detection of endogenous Cdc42, with or without RhoA biosensor induction. **e**, Quantification of (**d**); induced expression of the RhoA biosensor does not affect the relative expression levels of endogenous Cdc42 (N = 3 experiments). **f**, Western blot detection of endogenous Rac1, with or without RhoA biosensor induction. **g**, Quantification of (**f**); induced expression of the RhoA biosensor does not affect the relative expression levels of endogenous Rac1 (N = 3 experiments). **h**, β-Actin loading control for the Western blots in (**a**), (**d**), and (**f**). Two-sided Student's t-test, paired-analysis was used for panels (**c**), (**e**) and (**g**).

nature portfolio

Corresponding author(s): 0vijit Chaudhuri

Last updated by author(s): July 31, 2023

Reporting Summary

Nature Portfolio wishes to improve the reproducibility of the work that we publish. This form provides structure for consistency and transparency in reporting. For further information on Nature Portfolio policies, see our Editorial Policies and the Editorial Policy Checklist.

Statistics

For all statistical analyses, confirm that the following items are present in the figure legend, table legend, main text, or Methods section.

n/a	Confirmed	
☐	☒	The exact sample size (*n*) for each experimental group/condition, given as a discrete number and unit of measurement
☐	☒	A statement on whether measurements were taken from distinct samples or whether the same sample was measured repeatedly
☐	☒	The statistical test(s) used AND whether they are one- or two-sided *Only common tests should be described solely by name; describe more complex techniques in the Methods section.*
☒	☐	A description of all covariates tested
☐	☒	A description of any assumptions or corrections, such as tests of normality and adjustment for multiple comparisons
☐	☒	A full description of the statistical parameters including central tendency (e.g. means) or other basic estimates (e.g. regression coefficient) AND variation (e.g. standard deviation) or associated estimates of uncertainty (e.g. confidence intervals)
☐	☒	For null hypothesis testing, the test statistic (e.g. *F*, *t*, *r*) with confidence intervals, effect sizes, degrees of freedom and *P* value noted *Give P values as exact values whenever suitable.*
☒	☐	For Bayesian analysis, information on the choice of priors and Markov chain Monte Carlo settings
☒	☐	For hierarchical and complex designs, identification of the appropriate level for tests and full reporting of outcomes
☒	☐	Estimates of effect sizes (e.g. Cohen's *d*, Pearson's *r*), indicating how they were calculated

Our web collection on statistics for biologists contains articles on many of the points above.

Software and code

Policy information about availability of computer code

Data collection	1. Leica SP8 (Leica confocal microscopy images). 2. TA instruments (acquisition of rheometry data). 3. Nikon Ti2-E (Nikon confocal microscopy images).
Data analysis	1. Graphpad Prism 9.1.0 (used for plotting all graphs and statistical analysis). 2. Imaris 9.9.0 (used for cell tracking). 3. Matlab R2022a (used for analyzing raw data before plotting in Prism). 4. ImageJ v2.9.0 (used for displaying immunohistochemistry staining images). 5. COMSOL Version 6.0 (for simulations) 6. Adobe Illustrator 2022 and 2023 (used for figure preparation). 7. Microsoft Excel version 16.14 (data handling).

For manuscripts utilizing custom algorithms or software that are central to the research but not yet described in published literature, software must be made available to editors and reviewers. We strongly encourage code deposition in a community repository (e.g. GitHub). See the Nature Portfolio guidelines for submitting code & software for further information.

Data

Policy information about availability of data

All manuscripts must include a data availability statement. This statement should provide the following information, where applicable:

- Accession codes, unique identifiers, or web links for publicly available datasets
- A description of any restrictions on data availability
- For clinical datasets or third party data, please ensure that the statement adheres to our policy

Source data for each figure is provided. Raw images are available upon request due to the large file sizes of images.

Human research participants

Policy information about studies involving human research participants and Sex and Gender in Research.

Reporting on sex and gender	N/A
Population characteristics	N/A
Recruitment	N/A
Ethics oversight	N/A

Note that full information on the approval of the study protocol must also be provided in the manuscript.

Field-specific reporting

Please select the one below that is the best fit for your research. If you are not sure, read the appropriate sections before making your selection.

☒ Life sciences ☐ Behavioural & social sciences ☐ Ecological, evolutionary & environmental sciences

For a reference copy of the document with all sections, see nature.com/documents/nr-reporting-summary-flat.pdf

Life sciences study design

All studies must disclose on these points even when the disclosure is negative.

Sample size	Sample size was determined by following the range of sample sizes from previous studies relevant to our work. These provided sufficient power for statistical analyses. This gave us confidence in the statistical power of our analyses. (Wisdom et al., Nat Comm, 2018)
Data exclusions	No data was excluded from the experiments.
Replication	All experiments were replicated from distinct samples at least 2-3 times and independent experiments performed on separate days. Great care was taken to minimize experimenter error.
Randomization	Materials used for making hydrogels were prepared from different batches. Hydrogels were deposited in wells in a randomized fashion. For imaging, multiple fields of view were randomly selected. Allocation for imaging was done randomly.
Blinding	Blinding was not relevant to the current work since the metrics are quantified and objectively analyzed.

Reporting for specific materials, systems and methods

We require information from authors about some types of materials, experimental systems and methods used in many studies. Here, indicate whether each material, system or method listed is relevant to your study. If you are not sure if a list item applies to your research, read the appropriate section before selecting a response.

Materials & experimental systems

n/a	Involved in the study
☐	☒ Antibodies
☐	☒ Eukaryotic cell lines
☒	☐ Palaeontology and archaeology
☒	☐ Animals and other organisms
☒	☐ Clinical data
☒	☐ Dual use research of concern

Methods

n/a	Involved in the study
☒	☐ ChIP-seq
☒	☐ Flow cytometry
☒	☐ MRI-based neuroimaging

Antibodies

Antibodies used: anti-laminin-5 (γ2 chain, clone D4B5, Millipore Sigma, #MAB19562, 1:500), anti-collagen-IV antibody (Sigma, #SAB4500369, 1:500), anti-non-muscle Myosin IIa antibody (Abcam, #ab55456, 1:100), anti-phospho-FAK antibody (Tyr 397, Invitrogen, #700255, 1:500), anti-E-cadherin (BD Biosciences, #610181, 1:100), anti-β4 integrin (Thermo Fisher. 1:500), Alexa Fluor 488 goat anti-mouse IgG2a (#A21131, 1:1000), Alex Fluor 488 goat anti-mouse IgG2b (#A21141, 1:1000), Alexa Fluor 647 goat anti-mouse IgG1 (#A21240, 1:1000), Alexa Fluor 647 goat anti-rabbit (#A21244, 1:1000).

Validation: All antibodies were validated by the manufacturer, and were used according to the manufacturer instructions.

Eukaryotic cell lines

Policy information about cell lines and Sex and Gender in Research

Cell line source(s)	MDA-MB-231, HEK293T, MCF10As were from ATCC;MCF10AT and MCF10CA1a were from Wakefield lab (NIH), and were authenticated previously in the following paper (https://www.jci.org/articles/view/18899) .
Authentication	Cell lines from ATCC were authenticated from manufacturer (ATCC). Authetication was performed by ATCC using quality control experiments and STR profiling; mycoplasma not detected by ATCC
Mycoplasma contamination	No further mycoplasma testing was performed.
Commonly misidentified lines (See ICLAC register)	None were used in this study